Geochronology, pyrite trace elements, and sulfur isotope geochemical characteristics of the Saibagou gold deposit in the eastern part of the northern Qaidam Basin

Jia Xing[1], Jianguo Wang[1]*, Jianbao Liu[2], Yanguang Liu[3], Kai Bian[4], Jianwei Liu[5], Lina Cai[6] and Shengyun Wei[1]

[1]Department of Geological Engineering, Qinghai University, Xining, China, [2]School of Environmental and Biological Engineering, Henan University of Engineering, Zhengzhou, China, [3]Institute of Hydrogeology and Environmental Geology, Chinese Academy of Geological Sciences, Shijiazhuang, China, [4]School of Earth Science and Engineering, Hebei University of Engineering, Handan, China, [5]Academic Affairs Office, Qinghai University, Xining, China, [6]The Second Geological Exploration Institute, Henan Geological Bureau, Zhengzhou, China

Introduction: The Saibagou gold deposit, located in the eastern part of the tectonic belt of the northern Qaidam Basin in western China, has its gold ore bodies strictly controlled by the regional fault system. Despite this understanding, there remain controversies surrounding the deposit's metallogenic epochs, sources of ore-forming materials, and properties of ore-forming fluids. To address these controversy, the metallogenic process of the Saibagou gold deposit can be further determined by analyzing the U-Pb ages of hydrothermal zircons in the gold-bearing quartz veins and investigating the trace element and sulfur isotope compositions of pyrite in the gold deposit.

Methods: This study does not focus on the mineral characteristics susceptible to interference by the metallogenic condition in gold ore bodies. Instead, it offers a detailed discussion on stable associated minerals and their indicative markers formed in the process of gold mineralization.

Results: The results of this study showed that the metallogenic process of the gold deposit can be categorized into the following stages: 1) quartz−pyrite veins, 2) milky-white quartz—pyrite—native gold veins, 3) hoary quartz—native gold—polymetallic sulfide veins. As indicated by the U-Pb ages of hydrothermal zircons in the gold-bearing quartz veins, the Saibagou gold deposit has two metallogenic ages, namely, 423.91 ± 4.5 Ma (the Silurian) and 470.18 ± 4.92 Ma (the Ordovician).

Discussion: The Silurian metallogenic age, predominates and nearly aligns with the expansion of the regional NWW-trending brittle-ductile shear zone, followed by the Ordovician metallogenic age. Data on the trace elements and sulfur isotopes of pyrite, show that the Saibagou gold deposit has similar pyrite compositions in the three metallogenic stages. Gold in the deposit primarily occurs as native gold or minor petzite inclusions and has a very low lattice gold concentration. As indicated by the concentrations of elements such as Co, Ni, and as in the pyrite, as well as the variation range of $\delta^{34}S$ values, the

ore-forming fluids were derived from low-temperature arsenic-bearing acidic magmas. In addition, the primary ore-forming materials appear to encompass mantle-derived materials from the deep earth.

1 Introduction

Gold, as one of the world's most important strategic resources, plays an irreplaceable role in both industrial production and daily life (Chen et al., 2023). The tectonic belt of the northern Qaidam Basin, located at the northeastern margin of the Tibetan Plateau, is one of the most potential gold metallogenic areas in western China. This tectonic belt is characterized by frequent magmatic activities during the Lüliangian, Caledonian, Variscan, Indosinian, and Yanshanian periods and host fault structures, suggesting superior metallogenic conditions (Zhang D. Q. et al., 2009; Cai et al., 2019; Liu et al., 2021). Figure 1A illustrates thegeotectonic framework of western China, while Figure 1B shows the regional geological map of the northern margin of the Qaidam Basin and the distribution of typical gold deposits at the margin. The tectonic belt can be divided into eastern and western parts based on the occurrence conditions of gold deposits. In the eastern part, the Saibagou gold deposit stands out as the only medium-sized deposit currently identified (Zhang et al., 2018), while other gold deposits are small in scale. The gold mineralization of the Saibagou gold deposit is very closely linked to the development of multistage hydrothermal systems. As the largest gold deposit in the eastern part of the tectonic belt, the Saibagou gold deposit mainly occurs in the Early Paleozoic metavolcanic Tanjianshan Group. Its gold ore bodies are strictly controlled by regional deep faults and ductile-brittle shear zones. Among them, the shallow ore bodies predominantly consist of ores from gold-bearing quartz veins, while the deep ore bodies are largely composed of altered rock ores or a combination of both the aforementioned ores and altered rock ores (Tang et al., 2021a). Although studies have explored the metallogenic regularity of this gold deposit, most research has focused on the increase in peripheral resources in the Saibagou gold deposit, and studies on the metallogenic age, sources of ore-forming materials, and fluid properties of the deposit remain scarce (Zhang et al., 2001; Feng et al., 2002; Tang et al., 2021b). Some scholars have carried out sericite Ar-Ar isotopic dating, Rb-Sr isochron dating and zircon U-Pb dating on different surrounding rocks of the Saibagou gold deposit, but fail to achieve satisfactory research results. It can only be roughly inferred that the metallogenic age of the Saibagou gold deposit liesbetween the Ordovician and Silurian, and its formation is related to the subduction and collision between the Qaidam and Oulongbuluke blocks (Feng et al., 2002; Tong et al., 2009; Wu et al., 2022).

Some researchers proposed that the Ar, Rb, and Sr systems in the altered minerals (e.g., sericite) that are closely related to gold mineralization are susceptible to disturbances during their mineralization. As a result, their internal isotope systems would change, and, accordingly, dating results, will deviate and cannot accurately reflect the formation age of gold (Clauer et al., 1992; Luo

et al., 2000). Zircons, a common accessory mineral, are known for their high chemical stability (Smythe and Brenan, 2016; Li C. et al., 2022). Among them, Hydrothermal zircons formed either directly in saturated fluids or after transformation by fluid alterations, and their formation temperatures reflect the temperatures of two stages, namely, the magmatic stage and the mesothermal hydrothermal stage of the late magmatic process (Schaltegger, 2007). Therefore, hydrothermal zircons are frequently employed to constrain the timing of gold mineralization. As indicated by a study of zircons in gold-bearing quartz veins in the Abitibi green schist belt in Canada (Claoue et al., 1990; Claoue et al., 1992; Kerrich and Kyser, 1994), hydrothermal zircons and hydrothermal minerals such as gold and quartz were formed simultaneously under the same conditions (260–380°C, about 200 MPa). Subsequently, native gold grains and primary fluid inclusions were found in these zircons, and thus the gold mineralization age was successfully determined. It has been reported that many achievements have been made in determining the formation ages of hydrothermal gold deposits using hydrothermal zircons (Gao et al., 2021; Huang et al., 2021; Ma et al., 2022). Therefore, hydrothermal zircon dating can be used to accurately determine the metallogenic ages of hydrothermal gold deposits.

Presently, there are still some controversies about the sources of ore-forming materials and the properties of ore-forming fluids during the mineralization of the Saibagou gold deposit. Some scholars believed that the magmatic-hydrothermal fluids provided by Early Silurian granite intrusion activated and extracted the materials of the metavolcanic Tanjianshan Group. This led to the formation of ore-bearing hydrothermal solutions, which precipitated and formed ores in the tensional parts of early-formed shear zones (Fu and Li, 1998). Alternatively, other scholars argued that the water in the deep suites of the earth and meteoric water activated and extracted ore-forming elements from the surrounding rocks of the mining area under the action of collisional orogenesis. Subsequently, these ore-forming elements precipitated to form ores in the parts subjected to the tectonic transformation of shear zones (Feng et al., 2002). Nevertheless, some scholars attributed the Saibagou gold deposit to mixed hydrothermal mineralization (Zhang et al., 2001).

These different conclusions were proposed primarily due to the complex evolutionary process of the tectonic belt of the northern Qaidam Basin. Previousfluid inclusion tests can result in deviations of interpretation results due to the presence of structurally bound water in the fluid inclusions (Vallance et al., 2004; Baatartsogt et al., 2007). Certain studies show that quartz veins can trap multi-generation fluids, some of which may be unrelated to gold mineralization, thus leading to deviations in the H-O isotope test results of quartz veins (Goldfarb and Groves, 2015). In sum, there are still discrepancies in the understanding of the sources of ore-
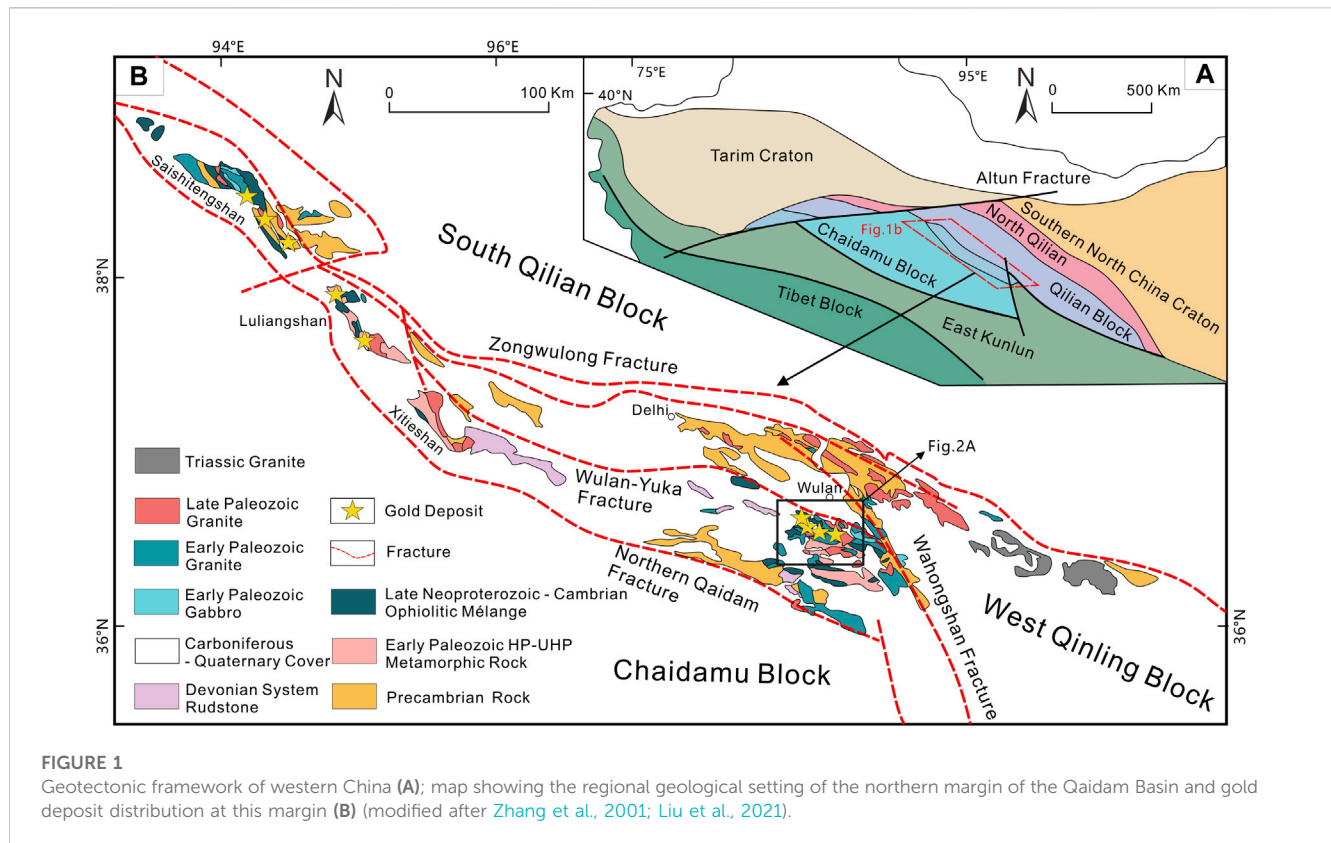
FIGURE 1
Geotectonic framework of western China **(A)**; map showing the regional geological setting of the northern margin of the Qaidam Basin and gold deposit distribution at this margin **(B)** (modified after Zhang et al., 2001; Liu et al., 2021).

forming materials and the properties of ore-forming fluids in the Saibagou gold deposit. These disagreements to a certain extenthave constrained the development of the metallogenic theory of gold deposits in the study area. Compared to quartz, pyrite—the major carrier of gold in the Saibagou gold deposit—is the metal sulfide that is the most closely related to gold mineralization, and its chemical composition provides information on the formation environment of pyrite (Franchini et al., 2015; Gregory et al., 2016; Zheng et al., 2020). Therefore, analyzing the trace elements and S isotopes in pyrite of gold ores in gold-bearing quartz veins can provide more reliable evidence for the sources of gold ore-forming materials and the properties of ore-forming fluids.

This study examined the Saibagou gold deposit, which is the largest gold deposit in the tectonic belt of the northern Qaidam Basin. It employed more reasonable test methods (U—Pb dating, trace elements, and sulfur isotopes) for suitable test subjects (hydrothermal zircon and pyrite). The purpose is to further explore the metallogenic ages, the sources of ore-forming materials, and the properties of ore-forming fluids of the Saibagou gold deposit. This study holds significant reference values for further theoretical breakthroughs and the optimization of favorable target areas in this region. Hydrothermal zircon U-Pb dating, as well as the analyses of the trace elements and sulfur isotope compositions of pyrite, allows us to accurately constrain the metallogenic age, sources of ore-forming materials, and fluid properties of the Saibagou gold deposit. Therefore, research on the metallogenic age, sources of ore-forming materials, and fluid properties of the Saibagou gold deposit has important implications

for the theory of gold deposits and the development of critical metal deposits in this region.

2 Regional geological setting

The study area situated within the Qinling-Qilian-Kunlun fold mountain system in western China. Regarding the regional geotectonic setting, it extends across the Tanjianshan magmatic arc, the ophiolite melanges at the northern margin of the Qaidam Basin, and the Oulongbuluke microcontinent, lying at the intersection of the Wahongshan-Wenquan fault and the Oulongbuluke-Maoniushan fault (Figure 1) (Liu et al., 2021). This area has experienced continental breakup, the formation and subduction of oceanic basins, continent-continent collisional orogenesis, and large-scale magmatism (Wu et al., 2006; Song et al., 2014; Shao et al., 2018), forming a significant gold, copper, and zinc polymetallic ore concentration area in western China. Chronologically, theoutcrops in the study area include the Lower Proterozoic Dakendaban Group (Pt_1dk), the Upper Ordovician Tanjianshan Group (Q_3tn), the Upper Devonian Maoniushan Formation (D_3m), and the Quaternary System (Q) (Feng et al., 2002). The Dakendaban Group is composed primarily of greenschist-facies gneisses, while the Tanjianshan Group consists mainly of greenschists and small quantities of hornblendites, basalts, quartzites, marbles, schistositized andesites, and pyroclastics interbedded with mica-quartz schists. The Maoniushan Formation is comprised primarily of giant-to coarse-grained gravel-grade molasse suites, and the Quaternary strata
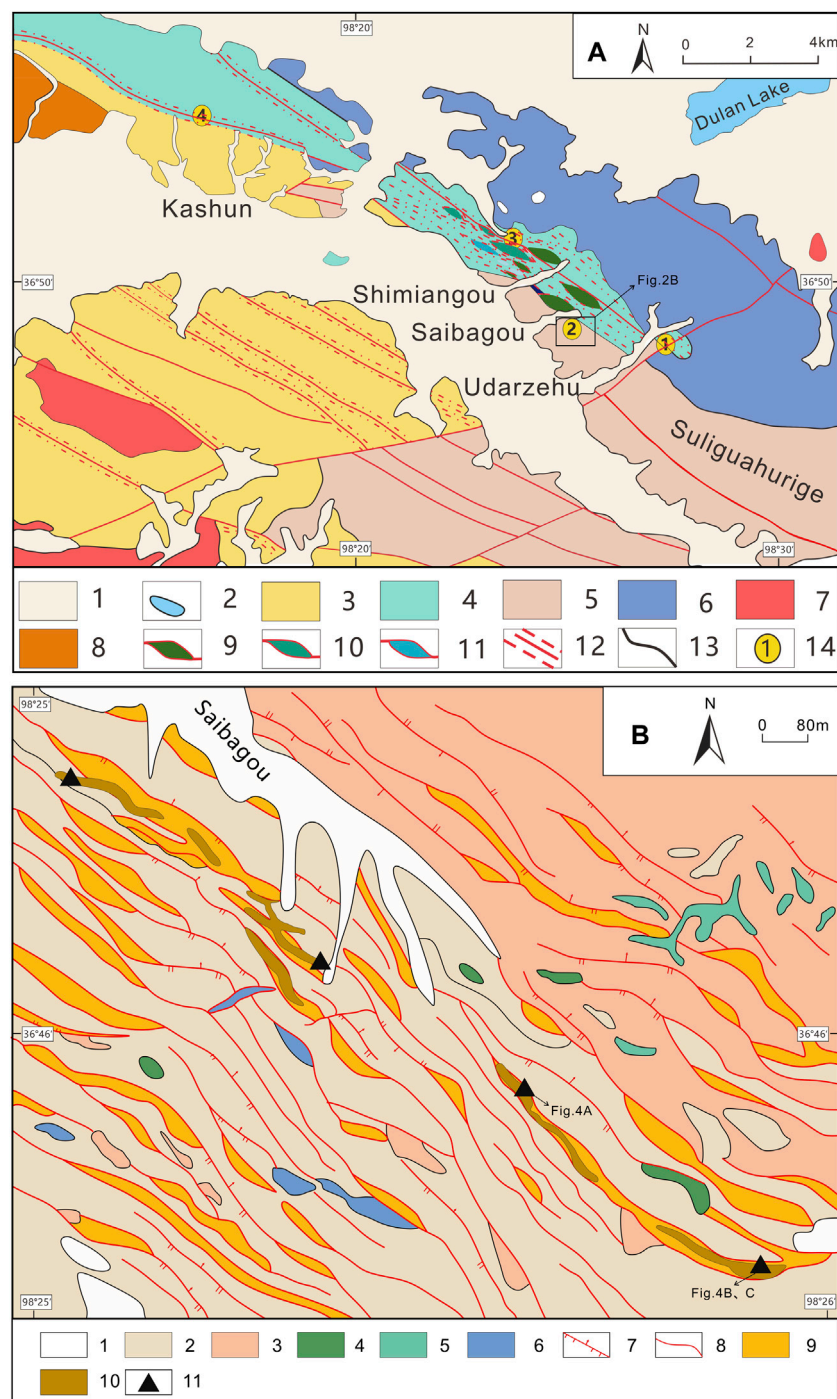
FIGURE 2
Regional geological map of Saibagou **(A)**; Geological map of the Saibagou gold mining area **(B)**. (modified after Feng et al., 2002; Liu et al., 2005; Tang et al., 2021a, b). Note: **(A)** 1 Quaternary; 2 Dulan Lake; 3 Tanjianshan Group; 4 Ophiolite melange; 5 Middle Ordovician granite; 6 Early Silurian granite; 7 Early Carboniferous granite; 8 Middle-Late Devonian Maoniushan Formation; 9 Gabbro; 10 Plagioclase amphibolite; 11 Metasiltstone; 12 Fault and mylonite zone; 13 Geological boundary; 14 Gold deposit (1 Udarzehu gold deposit, 2 Saibagou gold deposit, 3 Tuoxingou gold deposit, 4 Kashun gold deposit). **(B)** 1 Quaternary; 2 Granodiorite; 3 Fine-grained diorite; 4 Granite porphyry; 5 K-feldspar granite; 6 Diorite porphyrite; 7 Measured and inferred reverse faults; 8 Surveyed and inferred unknown faults; 9 Mylonite zone; 10 Gold ore body; 11 Partial sampling points.

predominantly comprise alluvial-proluvial gravel deposits (Figure 1) (Tang et al., 2021a). Fault structures, mainly consisting of two sets of faults with notable geological significance (NWW-and NE-trending faults), have extensively developed in the region. The NWW-

trending faults serve as the most important ore-controlling faults, playing a significant role in the formation and distribution of gold ore bodies in the study area. In contrast, the NE-trending faults, which formed post-mineralization, have made limited contributions
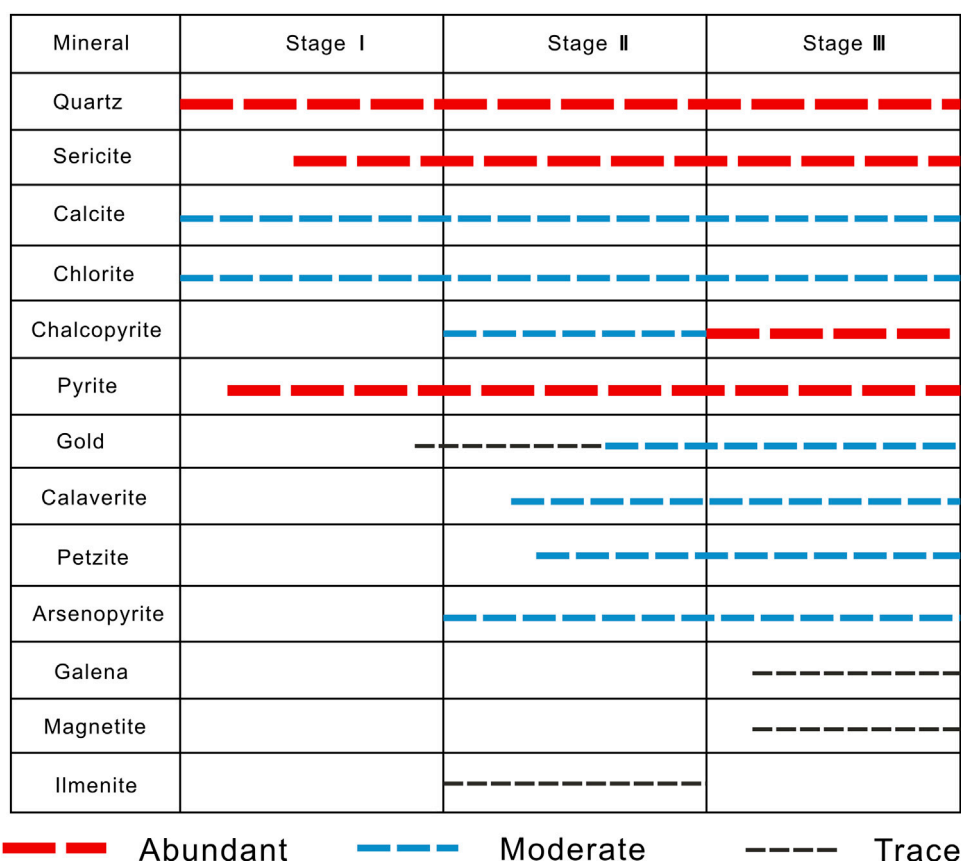
FIGURE 3
Mineral formation sequence of the Saibagou gold deposit.

to the formation of gold deposits in the study area (Feng et al., 2002). The study area experienced intense magmatic activity during the Lüliangian, Caledonian, Variscan, Indosinian, and Yanshanian periods, with the Variscan, period undergoing the most extensive and intense activity (Tong et al., 2009). Intrusions formed by magmatic activity have widely developed in the gold mining area. Their emplacement was affected by the NWW-trending faults, resulting in the development of various plutons in the NWW direction. The lithologies in the study area include medium-and fine-grained granites, fine-grained diorites, medium-grained monzonites, and gabbro, from south to north.

3 Geological setting of the Saibagou gold deposit

The gold ore bodies in the Saibagou gold deposit have mostly developed in the NWW-trending brittle-ductile shear zone (Figure 2A) (Liu et al., 2005). They occuras veinlets and branched veins and in irregular and lenticular forms within plagiogranites and granodiorites. Along their strikes, the ore bodies exhibit phenomena such as pinchout, recurrence, expansion, and contraction (Figure 2B). The ore bodies display significant attitude variations and have a NW-SE strike and a NE dip direction. A few ore bodies show bending deformation due to the surface gravitational creep. As a result, the ore bodies near the surface incline SW and those in deep partsincline NE. The gold ores in the study area are predominantly of quartz vein type and altered rock type (Tong et al., 2009).

The ore minerals in the Saibagou gold deposit are mostly native gold, pyrite, chalcopyrite, and petzite, while the primary gangue minerals include quartz, with minor amounts of plagioclase, sericite, and chlorite. The ores show the characteristics of a disseminated structure, with gold minerals mainly present in particulate or fine-grained native gold forms. Native gold mostly occurs as fine or irregular grains within the interstices of gangue minerals, forming intergranular gold with grain sizes of 0.005–0.025 mm. Some of the native gold is filled among the rock fractures, forming fissure gold. Besides, a small amount of inclusion gold also exists in the pyrite (Liu et al., 2005). The surrounding rock alterations, such as silicification and alterations of pyrite, limonite, and sericite, have played a significant role in the formation of the gold ore bodies in the Saibagou gold deposit. Based on field surveys of the distribution of ore-bearing quartz veins, the paragenetic relationships of minerals, and previous study data (Zhang et al., 2001; Feng et al., 2002; Liu et al., 2005; Tang et al., 2021b), it is finally determined that the Saibagou gold deposit has three metallogenic stages (Figure 3), namely, the formation stages of quartz-pyrite veins, milky-white quartz—pyrite—native gold veins, and hoary quartz—native gold—polymetallic sulfide veins.
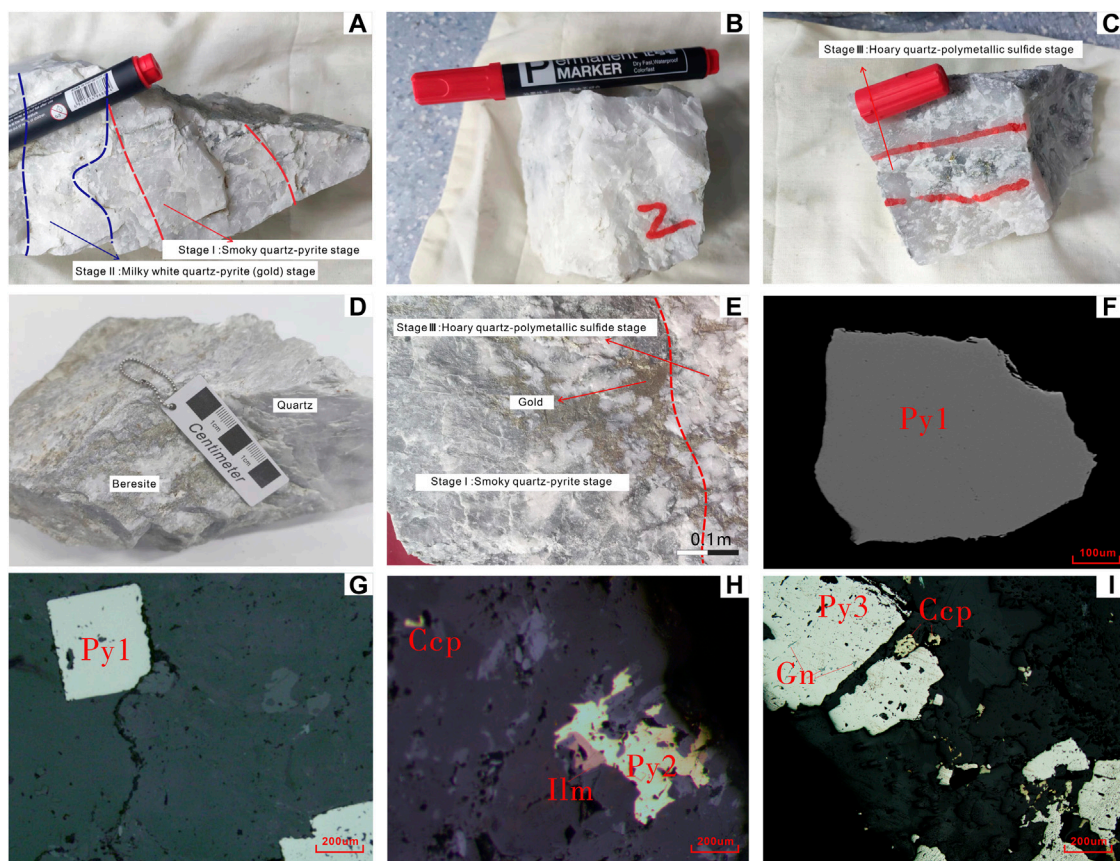
FIGURE 4
Hand specimens and microphotographs for ores from the Saibagou gold deposit. Ores of the quartz–pyrite veins of stage I and the milky-white quartz—pyrite—native gold veins of stage II **(A)**; ores of the milky-white quartz—pyrite—native gold veins of stage II **(B)**; ores of the hoary quartz—native gold—polymetallic sulfide vein ore of stage III **(C)**; Quartz vein intruding into beresite **(D)**; the gold ore and native gold of stages 1 and 3 **(E)**; pyrite grains of Py1 **(F, G)**; pyrite grains and other metal minerals of Py2 **(H)**; pyrite grains and other metal minerals of Py3 **(I)**. Note: Py: pyrite; Ccp: chalcopyrite; Ilm: ilmenite; Gn: galena.

Stage I: the formation stage of quartz-pyrite veins. This stage is characterized by the presence of a small amount of pyrite and smoky quartz veins, unevenly scattered medium and coarse-grained pyrite in quartz veins or rock fractures, the absence of native gold, and commonly occurring sericite and pyrite alterations (Figure 4A).

Stage II: the formation stage of milky-white quartz—pyrite—native gold veins. Compared with stage I, the milky-white quartz formed at stage II has significantly coarser grains and the pyrite formed at stage II has finer grains and a higher concentration. Metal minerals such as native gold, petzite, and chalcopyrite began to appear. The major alteration types at this stage still include sericite and pyrite alterations (Figures 4A,B).

Stage III: the formation stage of hoary quartz—native gold—polymetallic sulfide veins. This stage is characterized by the presence of pyrite aggregates coarse-grained pyrite, the extensive presence ofchalcopyrite, and the presence of polymetallic sulfide veins of galena and sphalerite. Furthermore, native gold and petzite of this stage mostly developed along rock fractures and between minerals. All these characteristics

mark this stage as the most crucial stage for Saibagou gold mineralization. The gold ores formed in this stage comprise the main body of the Saibagou gold deposit, and sericite and pyrite alterations continued to be widely distributed at this stage (Figures 4C–E).

As the main sulfide mineral in the Saibagou gold deposit, pyrite is the main carrier of gold in the gold deposit and is the most closely related to gold. Based on the metallogenic stages and mineral paragenesis, the pyrite in the Saibagou gold deposit can be categorized into three major types, namely, Py1, Py2, and Py3. Py1 is medium- and coarse-grained idiomorphic pyrite. This type of pyrite is scattered in quartz veins and has coarse grains with diameters of about 4 mm. Py1 is not accompanied by other sulfides and does not exhibit internal deformation. Some Py1 occasionally contains a few quartz inclusions (Figures 4F,G). Py2 is hypidiomorphic to idiomorphic pyrite with grain diameters of 0.5–2 mm, coexisting with a small amount of chalcopyrite and ilmenite (Figure 4H). Py3 is idiomorphic to hypidiomorphic pyrite and is accompanied by polymetallic sulfides such as chalcopyrite, galena, and sphalerite (Figure 4I).

4 Samples and test methods

4.1 Sample preparation and test process

Samples were collected from the gold-bearing quartz vein-type ores located in the NWW-trending brittle-ductile shear zone of the Saibagou gold deposit. These ores have plagiogranites or granodiorites as the surrounding rocks and exhibit an average gold grade of 5 g/t. A total of 25 pieces of quartz vein-type gold ores were collected from the Saibagou gold deposit, which was approximately 145 kg. During the collection of ore samples from mining roadways, most of the surrounding rocks attached to the gold-bearing quartz vein-type ores were removed in advance, the total weight of 145 kg. Among these samples, two samples were utilized to prepare polished thin sections for observational purposes, and the remaining 23 samples were used for sorting out zircons and pyrite. All the samples were processed and analyzed at the Wuhan Sample Solution Analytical Technology Co., Ltd. in Hubei Province, China. A total of 1650 various zircon grains and several pyrites were obtained. Tests and analyses were conducted on these samples in this study, including the cathodoluminescence (CL) imaging, U-Pb isotopic dating, and trace element analysis of zircons, as well as the backscattering (BSE) imaging, S isotope analysis, and trace element analysis of pyrite. Zircon CL images of all zircon grains were obtained and pyrite BSE imaging was conducted for some pyrite grains. All obtained microphotographs were carefully observed and tested to contribute to the broader understanding of the Saibagou gold deposit's geological characteristics.

4.2 Test methods

The zircon CL images were obtained using a high-vacuum scanning electron microscope (JSM-IT300) equipped with a Delmic sparc CL probe. This instrument operated at a voltage of 0.5–30 kV, a filament emission current of 72 μA, an accelerating voltage of generally 20–30 kV in spectral analysis and tests, and a working distance of 9.5–10.5 mm. Zircon U-Pb isotopic dating and the determination of the trace element concentrations of zircons were simultaneously completed using laser ablation inductively coupled plasma mass spectrometry (LA-ICP-MS) at the Wuhan Sample Solution Analytical Technology Co. Ltd. (Zong et al., 2017). A GeolasPro laser ablation system was used for laser sampling. During the laser ablation, helium was used as the carrier gas, argon was used as the make-up gas to adjust the sensitivity (Hu et al., 2015), and the laser beam spots and frequency were set at 32 μm and 5 Hz, respectively. Moreover, zircon reference material 91,500 and glass reference material NIST 610 were used as external standards for the fractionation corrections of zircon isotopes and trace elements, respectively. Each piece of the time-resolved analytical data included a blank signal of about 20–30 s and sample signals of 50 s. The data were processed using the ICPMSDataCal (Liu et al., 2008; Liu et al., 2010) and IsoplotR software. LA-ICP-MS was used to conduct the *in situ* microanalysis of major and trace elements in pyrite, with the GeolasPro laser ablation system used for laser sampling under the same laser ablation conditions stated above. The glass reference materials NIST 610 and NIST 612 served as external standards for calibration, while no internal standard was

employed for calibration. To verify the reliability of the calibration method, USGS sulfide reference material MASS-1 was used to monitor standard samples. Each piece of time-resolved analytical data also included a blank signal of about 20–30 s and sample signals of 50 s and was processed using the ICPMSDataCal software.

The *in situ* microanalysis of the sulfur isotope ratio of sulfides in pyrite was conducted using laser ablation multi-collector inductively coupled plasma mass spectrometry (LA-MC-ICP-MS) (Fu et al., 2016), with a Geolas HD system used as the laser ablation system and a Neptune Plus multicollector ICP-MS employed for MC-ICP-MS. The laser ablation system utilized helium as the carrier gas, with analysis conducted in single-point mode. Large, large laser beam spots of 44 μm were used, alongside a low frequency of 2 Hz. Moreover, the system was designed to cover about 100 laser pulses for analysis. To guarantee stable signals at low frequencies, a signal smoothing device was employed, and the laser energy density was kept constant at 5.0 J/cm^2. A Neptune Plus mass spectrometer was adopted, which was equipped with nine Faraday cups and a 1011 Ω resistance amplifier. Among them, three Faraday cups (L3, C, and H3) were employed to simultaneously receive ^{32}S, ^{33}S, and ^{34}S signals. To increase the signal intensity, a high-performance combination of the Jet sample cone and the X-skimmer cone was used. Nitrogen (4 mL/min) was introduced into the plasma to reduce the interference from polyatomic ions. Moreover, the system operated in the medium resolution mode (about 5000), and the mass fractionation of sulfur isotopes was corrected using the SSB method. To prevent any potential matrix effects, the pyrite samples were calibrated using the pyrite reference material PPP-1.

5 Test results

5.1 Zircon U-Pb dating results

The zircon dating results and trace element analysis results of the selected gold ore samples are shown in Tables 1 and 2, respectively. A total of 50 survey points were selected for zircon U-Pb dating, with 35 representative survey points being determined after some points with a low degree of concordance were screened out. The zircons were divided into three groups according to their morphologies, CL images, ages, and trace element distribution (Figure 5). The first group of zircons was mainly short prismatic. They had a length of generally less than 150 μm and a width of less than 50 μm, with length-to-width ratios of 1:2–1:3. They exhibited intact crystal morphologies. In the CL images, they were gray or hoary and had irregular luminous areas. The zircons of the first group were rich in inclusions, and some of them were black and not luminous. They had Th concentrations of 200 ppm–2884 ppm, a U concentration of 157 ppm–3114 ppm, and Th/U ratios of 0.24–1.69 (average: 0.72), suggesting significant characteristics of hydrothermal origin (Rubatto and Hermann, 2003; Hoskin, 2005; Zhong et al., 2018). They had ^{206}Pb/^{238}U ages of 417–429 Ma and 455–485 Ma, with weighted averages of 423.91 ± 4.5 Ma (MSWD=1.1) and 470.18 ± 4.92 Ma (MSWD=3.7), respectively. The second and third groups of zircons were captured zircons. They were mostly short prismatic or granular. They had varying grain sizes, with lengths generally less than 100 μm (nearly 200 μm

TABLE 1 LA-ICP-MS zircon U-Pb dating results of the gold-bearing quartz veins in the Saibagou gold deposit.

Survey point	Trace element content (×10⁻⁶)				Isotope ratio				Age (Ma)				Degree of concordance (%)
	Th	U	Th/U	Pb*	^{207}Pb/^{235}U	±1σ	^{206}Pb/^{238}U	±1σ	^{207}Pb/^{235}U	±1σ	^{206}Pb/^{238}U	±1σ	
Group 1													
S1422	442	564	0.78	2.10	0.5473	0.0181	0.0668	0.0007	443	11.88	417	4.42	93%
S1423	219	310	0.71	1.06	0.5732	0.0182	0.0683	0.0008	460	11.74	426	4.72	92%
S1424	222	547	0.41	0.86	0.5108	0.0199	0.0678	0.0010	419	13.39	423	5.82	99%
S1425	200	459	0.44	1.20	0.5228	0.0186	0.0687	0.0008	427	12.40	429	4.86	99%
S191	37.1	157	0.24	0.00	0.4975	0.0221	0.0688	0.0010	410	14.96	429	5.96	95%
S222	2884	3114	0.93	0.86	0.6033	0.0117	0.0758	0.0009	479	7.43	471	5.28	98%
S223	632	869	0.73	1.15	0.6128	0.0155	0.0759	0.0009	485	9.77	472	5.55	97%
S32	195	234	0.84	7.44	0.5646	0.0723	0.0762	0.0013	454	46.92	473	7.52	95%
S2225	1422	840	1.69	4.63	0.5570	0.0158	0.0782	0.0009	450	10.34	485	5.38	92%
S2214	184	466	0.40	0.11	0.5942	0.0204	0.0732	0.0008	474	12.98	455	4.74	96%
Group 2													
S421	13.67	35.57	0.38	0.36	0.5370	0.0403	0.0732	0.0012	436	26.60	455	7.41	95%
S921	40.23	103.22	0.39	0.00	0.5557	0.0245	0.0747	0.0008	449	16.00	464	5.06	96%
S1321	80.24	242.72	0.33	0.00	0.5488	0.0274	0.0765	0.0011	444	17.93	475	6.43	93%
S324	48.36	112.84	0.43	0.46	0.5886	0.0237	0.0780	0.0009	470	15.14	484	5.53	97%
S1021	28.58	76.59	0.37	0.22	0.5921	0.0379	0.0802	0.0014	472	24.18	497	8.47	94%
S721	15.71	41.35	0.38	0.00	0.6324	0.0482	0.0774	0.0016	498	29.98	480	9.55	96%
S221	359.28	620.04	0.58	0.96	0.6254	0.0183	0.0770	0.0011	493	11.46	478	6.30	96%
S151	26.94	72.26	0.37	0.00	0.6456	0.0387	0.0774	0.0012	506	23.86	480	7.42	94%
S1621	42.59	88.70	0.48	0.93	0.6034	0.0332	0.0777	0.0011	479	21.06	483	6.43	99%
S141	118.93	232.22	0.51	1.25	0.6677	0.0250	0.0776	0.0009	519	15.24	482	5.48	92%
S2121	11.63	38.41	0.30	0.00	0.6733	0.0386	0.0772	0.0014	523	23.44	479	8.64	91%
S2223	263.35	331.04	0.80	0.51	0.6873	0.0450	0.0838	0.0024	531	27.06	519	14.44	97%
S2213	197.77	341.96	0.58	0.16	0.7288	0.0246	0.0902	0.0011	556	14.47	557	6.24	99%
S2021	64.25	145.52	0.44	0.44	0.6419	0.0235	0.0833	0.0010	504	14.52	516	5.69	97%
Group 3													
S521	69.17	249.75	0.28	0.36	1.1200	0.0290	0.1264	0.0012	763	13.91	767	6.66	99%
S2215	305.93	745.74	0.41	0.17	1.0623	0.0319	0.0992	0.0012	735	15.71	610	6.85	81%
S2322	82.79	540.91	0.15	0.17	1.0784	0.0282	0.1220	0.0012	743	13.78	742	7.03	99%
S14	58.67	260.53	0.23	0.00	1.4983	0.0412	0.1574	0.0024	930	16.74	942	13.35	98%
S231	9.73	485.25	0.02	1.34	1.4640	0.0317	0.1467	0.0014	916	13.08	882	8.14	96%
S122	23.93	48.43	0.49	0.00	3.9505	0.1473	0.2740	0.0039	1624	30.24	1561	19.80	96%
S121	54.43	69.55	0.78	0.37	4.3852	0.1251	0.2995	0.0030	1710	23.62	1689	14.99	98%
S126	31.54	121.82	0.26	0.00	4.3506	0.1493	0.2216	0.0043	1703	28.35	1290	22.81	72%
S81	73.20	56.47	1.30	4.27	10.1724	0.5067	0.4422	0.0151	2451	46.08	2360	67.55	96%

TABLE 2 Results of REE analysis of gold-bearing quartz veins in the Saibagou gold deposit.

Sample No.	La	Ce	Pr	Nd	Sm	Eu	Gd	Tb	Dy	Ho	Er	Tm	Yb	Lu	Y
Group 1															
S1422	24.8	87.3	7.4	30.9	10.0	0.9	28.6	8.8	96.4	35.3	157.2	33.5	309.7	64.2	1080.8
S1423	1.1	23.0	0.3	2.5	4.0	0.4	19.8	6.4	77.2	29.0	130.9	27.7	253.1	50.9	820.7
S1424	0.0	16.7	0.0	0.9	1.0	0.1	7.2	2.5	33.6	14.0	70.6	17.9	183.0	41.2	469.9
S1425	23.6	92.2	11.5	57.2	14.0	1.3	22.9	5.5	56.9	22.5	105.9	24.3	238.8	52.0	702.7
S191	0.0	1.3	0.0	0.8	1.4	0.4	12.4	5.1	70.3	27.9	131.8	27.6	257.7	53.9	859.4
S222	10.0	77.6	3.3	17.9	21.7	5.7	113.4	45.1	581.7	237.9	1159.0	256.7	2504.1	532.2	7060.1
S223	1.1	27.3	1.6	9.5	11.8	3.1	51.7	21.7	294.3	123.5	633.3	144.2	1449.0	321.4	3769.3
S32	1.5	79.1	2.6	19.8	22.9	6.5	72.4	23.6	217.7	65.0	263.9	49.3	446.4	83.9	1941.7
S2225	2.5	37.0	4.2	22.4	17.5	6.4	53.3	21.1	263.3	105.1	527.2	124.6	1262.8	277.5	3154.4
S2214	0.5	8.0	0.5	5.4	14.9	5.0	61.2	19.8	193.2	62.2	257.8	55.7	544.8	122.9	1806.4
Group 2															
S421	0.00	1.2	0.0	0.2	0.8	0.3	6.3	2.5	34.4	15.6	83.4	20.9	240.2	61.2	501.3
S921	0.01	2.5	0.0	0.3	0.9	0.4	8.8	3.9	59.0	28.5	159.0	40.8	462.5	119.1	925.9
S1321	0.14	3.1	0.1	2.0	4.8	0.1	27.6	9.4	111.6	40.2	170.2	34.0	293.1	58.8	1180.1
S324	0.00	3.3	0.0	0.7	1.4	0.7	12.5	5.5	81.4	38.2	210.1	51.1	572.7	145.6	1245.9
S1021	0.01	2.7	0.0	0.1	0.7	0.2	6.7	3.1	44.0	21.1	119.9	30.4	347.4	91.9	724.0
S721	0.01	1.6	0.0	0.1	0.4	0.3	5.0	2.4	36.0	17.0	97.5	25.6	292.8	77.6	586.6
S221	0.00	10.6	0.0	0.4	0.9	0.2	7.6	3.0	47.1	22.0	127.7	34.9	419.2	115.1	786.3
S151	0.12	2.1	0.0	0.2	0.9	0.3	7.3	2.9	44.3	21.9	123.4	31.1	360.2	95.0	737.9
S1621	0.00	2.7	0.1	0.8	1.8	0.6	14.1	5.8	78.1	35.3	188.6	46.3	514.3	131.4	1105.1
S141	0.00	7.0	0.0	0.4	2.1	0.4	15.3	7.2	108.6	54.0	285.5	70.6	765.3	192.0	1778.8
S2121	0.00	1.1	0.0	0.2	0.5	0.2	4.1	2.0	29.1	14.6	82.3	21.5	256.0	68.3	472.1
S2223	0.22	8.2	0.3	2.8	4.0	1.5	18.4	6.4	78.7	32.5	160.9	38.2	400.9	96.8	1017.1
S2213	0.18	12.2	0.2	1.5	2.7	1.0	18.2	7.3	105.6	46.3	242.9	57.2	606.2	140.8	1416.7
S2021	0.00	4.1	0.0	0.5	1.5	0.6	14.4	5.8	85.6	40.1	218.1	54.3	601.3	154.4	1279.3
Group 3															
S521	0.01	1.4	0.1	1.8	5.1	0.2	33.8	11.3	113.6	35.9	140.0	25.9	214.3	40.3	1064.4
S2215	0.33	9.9	0.1	1.1	2.7	0.5	12.4	5.5	74.6	31.7	161.1	38.0	380.4	81.5	1009.8
S2322	0.15	1.9	0.2	3.2	5.8	0.3	36.3	15.6	219.8	88.2	404.5	86.2	781.1	152.6	2557.5
S14	0.04	3.4	0.1	1.5	3.6	0.2	24.3	8.2	85.3	27.8	106.9	19.7	161.4	30.3	828.2
S231	0.01	0.3	0.0	0.1	0.9	0.1	8.3	3.7	30.2	5.5	14.4	2.5	19.8	4.1	182.0
S122	0.01	9.1	0.1	1.6	3.4	0.2	16.6	4.6	51.3	19.4	80.3	16.1	145.1	30.0	510.1
S121	0.05	11.3	0.3	5.4	7.1	0.3	28.1	8.5	89.3	31.8	132.3	25.5	221.3	42.9	884.3
S126	0.01	10.6	0.0	0.3	0.7	0.4	6.8	2.5	39.6	18.8	98.4	24.0	246.3	57.8	589.6
S81	0.01	10.7	0.0	0.3	0.7	0.3	5.2	1.9	21.5	8.4	41.1	8.4	78.6	16.8	273.5

Note: test unit×10^{-6}.

for some zircons), widths less than 50 μm (nearly 100 μm for some zircons), and length-to-width ratios of 1:2–1:1. They exhibited a high idiomorphic degree. The second group of zircons had a Th concentrations of 11.6 ppm–359 ppm, U concentrations of 35.6 ppm–620 ppm, and Th/U ratios of 0.30–0.80 (average: 0.45), implying significant characteristics of magmatic origin (Rubatto and
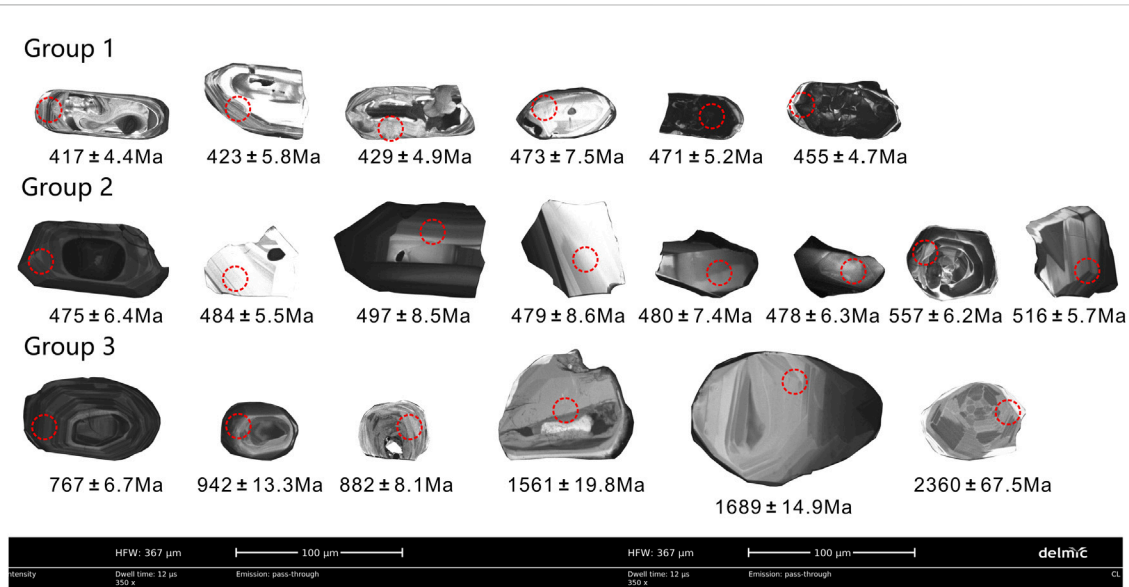
FIGURE 5
CL images of some zircons from the gold-bearing quartz veins of the Saibagou gold deposit.
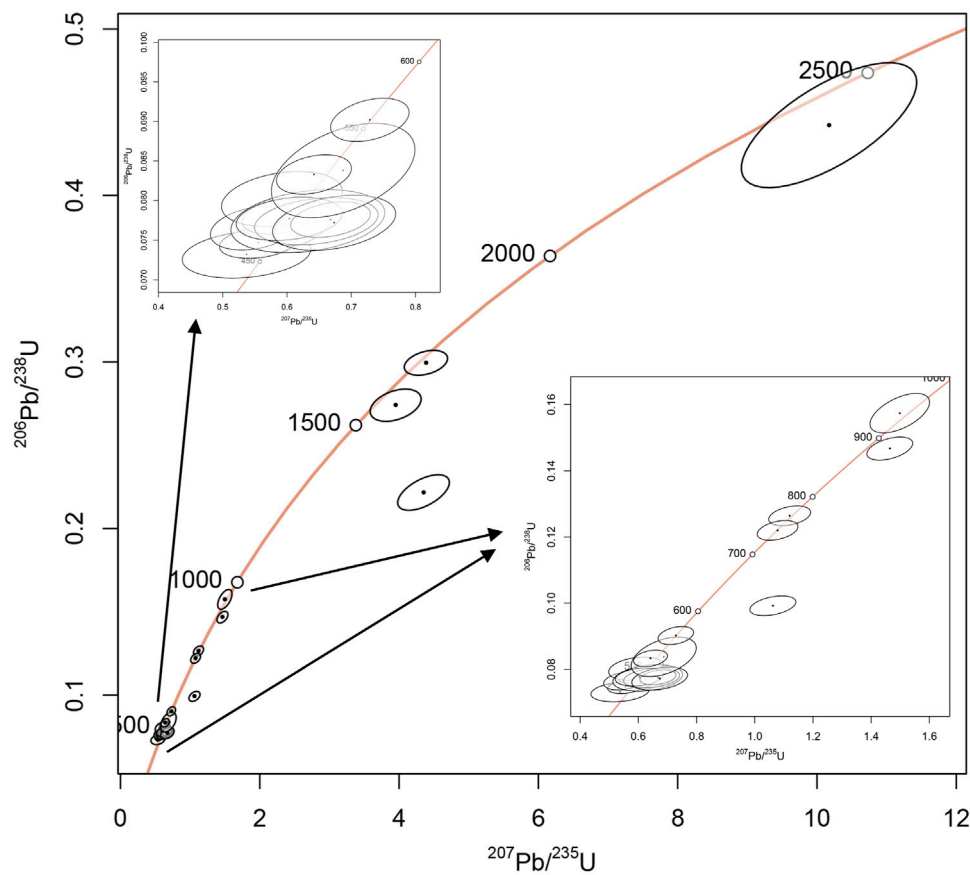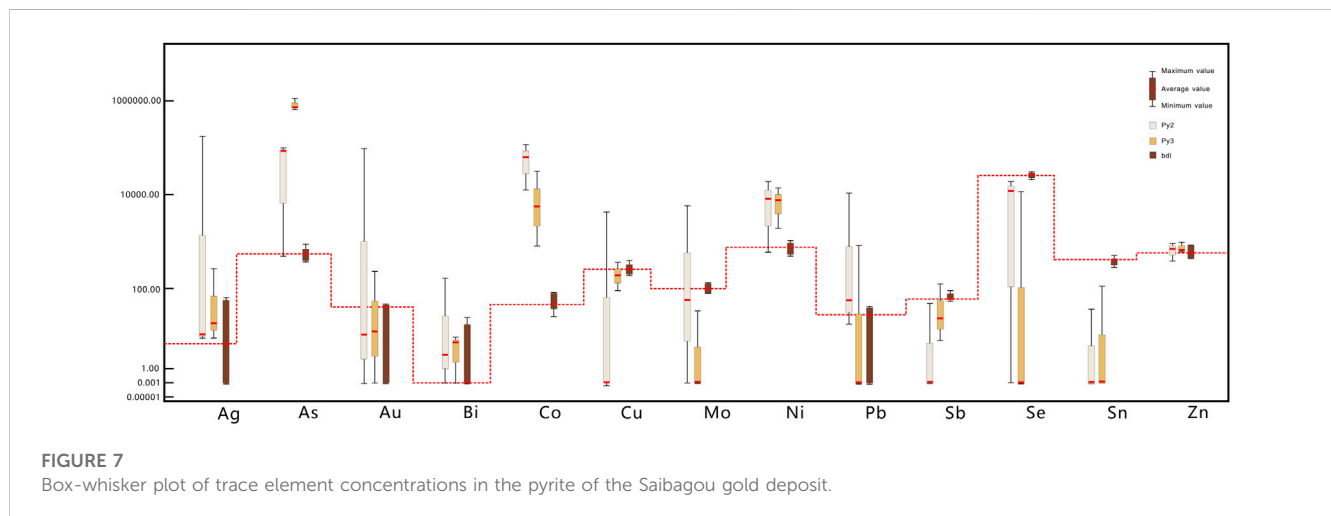

FIGURE 6
U-Pb concordia diagram of captured zircons from the gold-bearing quartz veins of the Saibagou gold deposit.

TABLE 3 Results of trace element analysis of pyrite in the gold-bearing quartz veins of the Saibagou gold deposit.

Survey point	Type of pyrite	Co	Ni	Cu	Zn	As	Se	Mo	Ag	Sn	Sb	Au	Pb	Bi
S107	Py2	12.68	0.60	—	bdl	bdl	bdl	0.06	bdl	bdl	—	—	0.02	—
S205	Py2	62.30	19.29	—	0.92	99.46	—	—	0.01	—	—	0.01	0.06	—
S307	Py2	115.10	8.25	4.26	0.70	85.16	bdl	5.79	171.76	—	bdl	95.19	10.89	0.17
S409	Py3	5.59	13.86	bdl	0.98	1106.78	—	—	0.01	—	bdl	—	—	—
S516	Py3	31.48	7.62	0.37	bdl	678.36	—	bdl	0.26	bdl	0.13	bdl	0.84	0.01
S602	Py3	0.82	1.96	bdl	bdl	697.57	bdl	—	0.02	—	bdl	bdl	—	0.01

Note: bdl denotes below the detection limit.

FIGURE 7
Box-whisker plot of trace element concentrations in the pyrite of the Saibagou gold deposit.

Hermann, 2003; Vavra et al., 1999; Belousova et al., 2006; Zhou et al., 2022). They had two sets of $^{206}Pb/^{238}U$ ages, namely, 455–497 Ma and 519–557 Ma, with a weighted average of 476.90 ± 3.92 Ma (MSWD = 2.6))for the former set. The weighted average of the latter set was not calculated due to the small number and the large value range of the survey points. The weighted average of the former set was consistent with the age of tonalite in the study area obtained in previous studies (Wu et al., 2022). The zircons with $^{206}Pb/^{238}U$ ages of 455–497 Ma were inferred to be zircon minerals trapped when ore-forming fluids upwelled and formed gold-bearing quartz vein-type ores. The third group of zircons had Th concentrations of 9.73 ppm–913 ppm, a U concentrations of 48.4 ppm–751 ppm, and a Th/U ratios of 0.15–1.30 (average: 0.56). They had scattered $^{206}Pb/^{238}U$ ages of 610–2360 Ma, which could be roughly divided into three age ranges, namely, 600–1000 Ma, 1500–2000 Ma, and greater than 2500 Ma (Figure 6). As revealed by the CL images, the third group of zircons exhibited significant core-mantle structures. The cores of the zircons were more luminous than the mantles and did not bear zoning textures. The mantles developed slightly oscillatory zoning or no zoning. Some zircons developed narrow altered rims, indicating that they might be magmatic zircons formed in the early stage and altered due to late metamorphism. According to the analysis, the age range of 600–1000 Ma is close to that (750–1000 Ma) of high to ultra-high-pressure metamorphic rocks in the northern Qaidam Basin (Yang et al., 2006; Zhang et al., 2006).

The zircons older than 1500 Ma might be derived from the ancient crystalline basement of the tectonic belt at the northern margin of the Qaidam Basin (Chen et al., 2007).

5.2 Composition of trace elements in pyrite

The three metallogenic stages of the Saibagou gold deposit are dominated by stages II and III, during which large quantities of gold elements precipitated and formed gold ores. Therefore, trace element analysis was conducted for the pyrite grains of the two stages. The trace element composition of pyrite in the gold ore samples is shown in Table 3. According to the test results, the pyrite in the Saibagou gold deposit has generally low concentrations of trace elements. Only a few elements, namely, Ag, As, Bi, Co., and Ni, had concentrations tested above their detection limits, while most trace elements showed concentrations below or near their detection limits (Figure 7). The pyrite in the gold ore samples was relatively enriched in trace elements Co., Ni, and As. Specifically, Py2 and Py3 had Co. concentrations of <63.36 ppm and <12.63 ppm, respectively, Ni concentrations of <9.38 ppm and <7.81 ppm, respectively, and As concentrations of <61.70 ppm and <827.57 ppm, respectively. For the pyrite of stages II and III, its Au concentrations were mostly close to the detection limit. An exception was observed at survey point S-307, where the Au

TABLE 4 δ³⁴S values of sulfides in the eastern and western parts of the northern margin of the Qaidam Basin.

Regional location	Sample No./ore deposit or lithology	Tested mineral	δ³⁴S/‰	Data sources
Eastern part of the northern margin of the Qaidam Basin tectonic belts	S017/quartz-pyrite veins of stage I	Pyrite	1.99	This study
	S09/quartz-pyrite veins of stage I	Pyrite	2.44	
	S119/milky-white quartz-pyrite (gold) veins of stage II	Pyrite	1.99	
	S203/milky-white quartz-pyrite (gold) veins of stage II	Pyrite	3.28	
	S415/hoary quartz - (gold) polymetallic sulfide veins of stage III	Pyrite	2.38	
	S620/hoary quartz - (gold) polymetallic sulfide veins of stage III	Pyrite	3.14	
	Saibagou gold deposit	Pyrite	0.5–3.92	Tang et al. (2021a)
	Gashun gold deposit	Pyrite	1.6–1.9	Zhang et al. (2001)
	Udarzehu gold deposit	Pyrite	1.3–3.4	Tang et al. (2021b)
	Surrounding rocks and post-metallogenic quartz	Pyrite	3.7–4.0	
Western part of the northern margin of the Qaidam Basin tectonic belt	Hongliugou gold deposit	Pyrite	3.9–4.4	Zhang (2017)
	Tanjianshan gold deposit	Pyrite	5.31–8.54	Guo and Shuwang (1998)
	Yuka gold deposit	Pyrite	0.5–7.4	Fan (2017)
	Qinglonggou gold deposit	Pyrite	5.0–11.0	Zhang (2017)

concentrations exceeded that of other points and the detection limit. This higher concentrations, which might be attributed to the presence of small native gold inclusions in the pyrite grains, agrees well with the ablation curve of LA-ICP-MS analysis.

5.3 Sulfur isotopic composition

As shown in the test results of sulfur isotopes (Table 4), the δ³⁴S values of pyrite of metallogenic stages I, II, and III varied slightly, in the ranges of 1.99 ‰–2.44‰ (average: 2.22‰; extreme differences: 0.45‰), 1.99 ‰–3.28‰ (average: 2.64‰; extreme differences: 1.29‰), and 2.38 ‰–3.14‰ (average: 2.76‰; extreme differences: 0.76‰), respectively. It is noteworthy that the average δ³⁴S value of pyrite in the Saibagou gold deposit varied with the metallogenic stages in theorder of $\delta^{34}S_I < \delta^{34}S_{II} < \delta^{34}S_{III}$. The main reason for this phenomenon is that the quantity of sulfur isotopes of pyrite increased with a decrease in temperature, as shown in the equilibrium fractionation curve of sulfur isotope exchange (Ohmoto, 1972). As the gold mineralization process continued, the ore-forming temperature decreased, leading to increased δ³⁴S values.

6 Discussion

6.1 Origin of zircons

All the hydrothermal zircons in the gold ore samples were characterized by relatively intact crystal forms, irregularly luminous areas, rich inclusions, and certain oscillatory and weak zoning textures. They are gray or hoary, with some beingblack and not luminous. These characteristics are significantly different from those of magmatic zircons, indicating that hydrothermal zircons were formed in saturated fluids or after transformation by fluid alterations during the formation of the gold-bearing quartz veins. This inference is consistent with the characteristics of hydrothermal zircons proposed by some researchers (Rubatto and Hermann, 2003; Hoskin, 2005; Zhong et al., 2018). Compared with the magmatic zircons in the gold ore samples, the hydrothermal zircons of the Saibagou gold deposit are significantly rich in LREEs (the first, second, and third groups of zircons had average LREE concentrations of 86.2 ppm, 7.44 ppm, and 11.99 ppm, respectively), especially rich in elements La and Ce (the first, second, and third groups of zircons had average La concentration of 6.53 ppm, 0.05 ppm, and 0.07 ppm, respectively and average Ce concentration of 44.49 ppm, 4.44 ppm, and 6.50 ppm, respectively), have high U and Th concentrations (the first, second, and third groups of zircons had an average U concentrations of 755.97 ppm, 177 ppm, and 286.49 ppm, respectively and average Th concentrations of 643.81 ppm, 94 ppm, and 78.82 ppm, respectively) and are rich in common lead (Pb; the first, second, and third groups of zircons had an average Pb concentrations of 1.94 ppm, 0.38 ppm, and 0.74 ppm, respectively). The hydrothermal zircons in the gold ore samples exhibit relatively flat distribution patterns of REEs, with weak or no Ce anomalies (Figure 8A). These characteristics are consistent with the results of the studies on the characteristics of hydrothermal zircons (Figure 8B) (Hoskin and Ireland, 2000; Rubatto, 2002; Geisler et al., 2003; Hoskin and
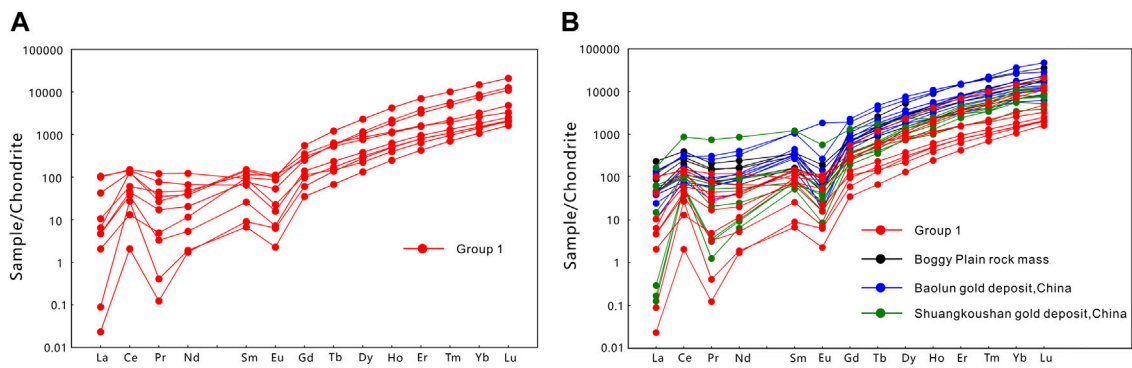
FIGURE 8
Chondrite-normalized REE patterns of hydrothermal zircons in the Saibagou gold deposit **(A)** and Chondrite-normalized REE patterns of hydrothermal zircons in other gold deposits **(B)**. (data on the Boggy Plain pluton after Kerrich and Kyser, 1994, data on the Baolun gold deposit after Zhang D. Q. et al., 2009, and data on the Shuangkoushan gold deposit after Yu et al., 2020).
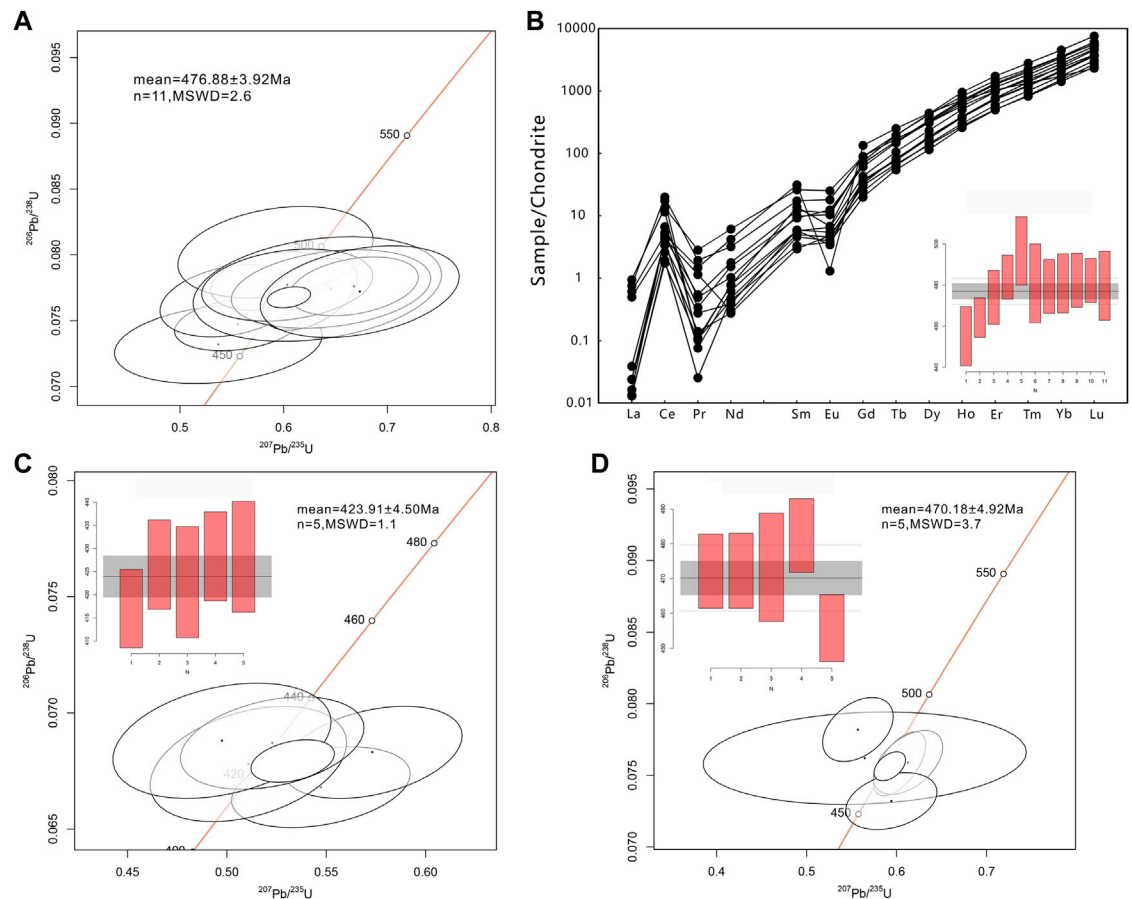

FIGURE 9
U-Pb concordia diagram **(A)** and chondrite-normalized REE patterns **(B)** of some magmatic zircons in the Saibagou gold deposit. U-Pb concordia diagrams of hydrothermal zircons from the Saibagou gold deposit **(C, D)**.

Schaltegger, 2003). However, they differ significantly from the REE distribution patterns of the magmatic zircons in the gold ore samples (Figures 9A,B).

The gold-bearing quartz vein-type ores of the Saibagou gold deposit have relatively high gold grades (average: 5 g/t). The formation conditions of these gold-bearing quartz veins, with

temperatures of 180 C–350 C and a pressure of 46 MPa (Liu et al., 2005), are similar to those of hydrothermal zircons in the Sudetic green schists in Poland (T: 207 C–300°C; P: 100 MPa) and the hydrothermal zircons in the gold-bearing quartz veins of the Shuangkoushan area at the northern margin of the Qaidam Basin (T: 280 C; P: 67.37 MPa) (Rubatto, 2002). As shown in the diagram of chondrite-normalized REE patterns, the hydrothermal zircons (group 1) in gold-bearing quartz veins exhibit consistent REE distribution with the hydrothermal zircons trapped in the Boggy Plain pluton in Australia, the ore-bearing quartz veins of the Shuangkoushan gold deposit at the northern margin of the Qaidam Basin in China, and gold ore bodies in the Baolun gold deposit in China (Figure 8B) (Hoskin, 2005; Zhang X. W. et al., 2009; Yu et al., 2020). This result indicates that the dating results of the hydrothermal zircons in the gold-bearing quartz vein-type ores can accurately represent the actual metallogenic age of the Saibagou gold deposit.

6.2 Metallogenic chronology

The dating results show that the hydrothermal zircons in the gold-bearing quartz veins have ages of 423.91 ± 4.5 Ma and 470.18 ± 4.92 Ma, indicating at least two distinct metallogenic periods of the Saibagou gold deposit. The metallogenic period is dominated by 423.91 ± 4.5 Ma (Figure 9C), which is consistent with the age of the regional NWW-trending ductile-brittle shear zone in the Saibagou area (426 ± 2 Ma) (Feng et al., 2002) but is slightly later than the ages of granodiorites (946 ± 26 Ma) and the Late Ordovician plagiogranites—the surrounding rocks of the ore bodies (Zhang et al., 2005). This result indicates that the formation of the gold-bearing quartz veins in the Saibagou gold deposit is closely related to the ductile-brittle shear zone in this area (Liu et al., 2005). Furthermore, the gold-bearing quartz vein-type ores are the major type of ores in the Saibagou gold deposit, and the gold ore bodies occur in the NWW-trending ductile-brittle shear zone. The ore body attitudes are roughly consistent with the characteristics of the ore deposi (e.g., fault strikes). Additionally, the dominant metallogenic period is slightly later than the ultrahigh-pressure metamorphic stage (428–435 Ma) of the northern margin of the Qaidam Basin (Chen et al., 2018a; Chen et al., 2018b). This result is consistent with the metallogenic regularity proposed by Goldfarb, which suggests that orogenic gold deposits were formed during or after the orogenic peak period (Goldfarb et al., 2001). Therefore, it can be inferred that the hydrothermal zircon age of 423.91 ± 4.5 Ma represents the primary metallogenic epoch of the Saibagou gold deposit.

The dating results also indicate a zircon age of 470.18 ± 4.92 Ma, which represents another metallogenic age of the gold deposits in the study area (Figure 9D). It is believed that the hydrothermal zircon dating results of the Saibagou gold deposit are reliable based on the morphologies, CL images, ages, and trace element distribution of zircons. Interestingly, the metallogenic age of 470.18 ± 4.92 Ma falls within the formation age (400–490 Ma) of the metavolcanic rock series in the Tanjianshan Group at the northern margin of the Qaidam Basin (Zhang et al., 2005; Cao et al., 2019). Moreover, this age belongs to the early stage of the Caledonian orogenic period and is close to the age (480 Ma) of the ophiolites in the Tanjianshan

Group in the Saibagou area (Cao et al., 2019). This metallogenic age is consistent with the established understanding of moderate-to-low-temperature magmatic-hydrothermal deposits (Ye et al., 2014). From these results, it can be inferred that during the subduction of the paleo-oceanic crust (South Qilian Ocean) toward the northern Qilian block, the crust was uplifted and thickened, and accordingly, fluids rose and metasomatized the upper mantle, leading to the partial melting of the lower crust. As a result, the metavolcanic rocks of the Tanjianshan Group with high background values of gold were formed. Concurrently, some ore-bearing hydrothermal fluids rose along regional deep faults, forming gold ore bodies in the local fractures derived near the deep faults.However, the formed gold ore bodies have a smaller scale and lower gold grades than those formed at 423.91 ± 4.5 Ma. Therefore, it can be concluded that the age 470.18 ± 4.92 Ma represents the secondary metallogenic period of the Saibagou gold deposit.

6.3 Occurrence state and fluid environment of trace elements in pyrite

As the most common gold-bearing sulfide in gold deposits, pyrite is an important mineral rich in multiple trace elementssuch as Co, Ni, Cu, Zn, As, and Au (Reich et al., 2005; Large et al., 2009; Berner et al., 2013). The differences in the degrees of enrichment of these trace elements in pyrite are frequently used to indicate the physical and chemical environment in which ore-forming materials were formed and to constrain the properties of ore-forming fluids (Liu et al., 2018; Li H. et al., 2022). In the Saibagou gold deposit, the Au concentrations in pyrite grains is generally near or below the detection limit, signifying an extremely low lattice gold concentration. Therefore, it can be inferred that the majority of the gold in the deposit occurs as native gold. However, an exceptional case is survey point S-307, where the pyrite displayed an unusually high Au concentrations, which considerably exceeded the values of other survey points and the detection limit. In addition, several extremely significant Au peaks appeared on the time-resolved LA-ICP-MS ablation curve of S-307 (Figure 10). Some researchers found that native gold is paragenetic with sulfide in the Saibagou gold deposit under the microscope (Liu et al., 2005). This finding suggests that the anomalous increase in the Au concentration of S-307 is likely due to the presence of small gold-bearing mineral inclusions in the pyrite rather than lattice gold. As shown in the time-resolved LA-ICP-MS ablation curves of pyrite, the Au signal exhibited very similar distribution characteristics to the Ag and Te signals, and the anomalous Au peaks tended to be accompanied by the anomalous peaks of Ag and Te. Given the mineral formation sequence in the Saibagou gold deposit, the small gold-bearing mineral inclusions in the pyrite could possibly be fine-grained petzite.

As shown by the time-resolved LA-ICP-MS ablation curves of pyrite, the Co, Ni, and As signals showed relatively stable intensities and similar distributions to the Fe signal. It can be inferred that Co, Ni, and As mainly infiltrated into pyrite grains through isomorphism. During metallogenic stages II and III, the pyrite had a stable As concentration in each epoch, and ferric sulfarsenide, such as arsenopyrite, appeared. Similar findings have also been reported by otherresearchers (Liu et al., 2005).
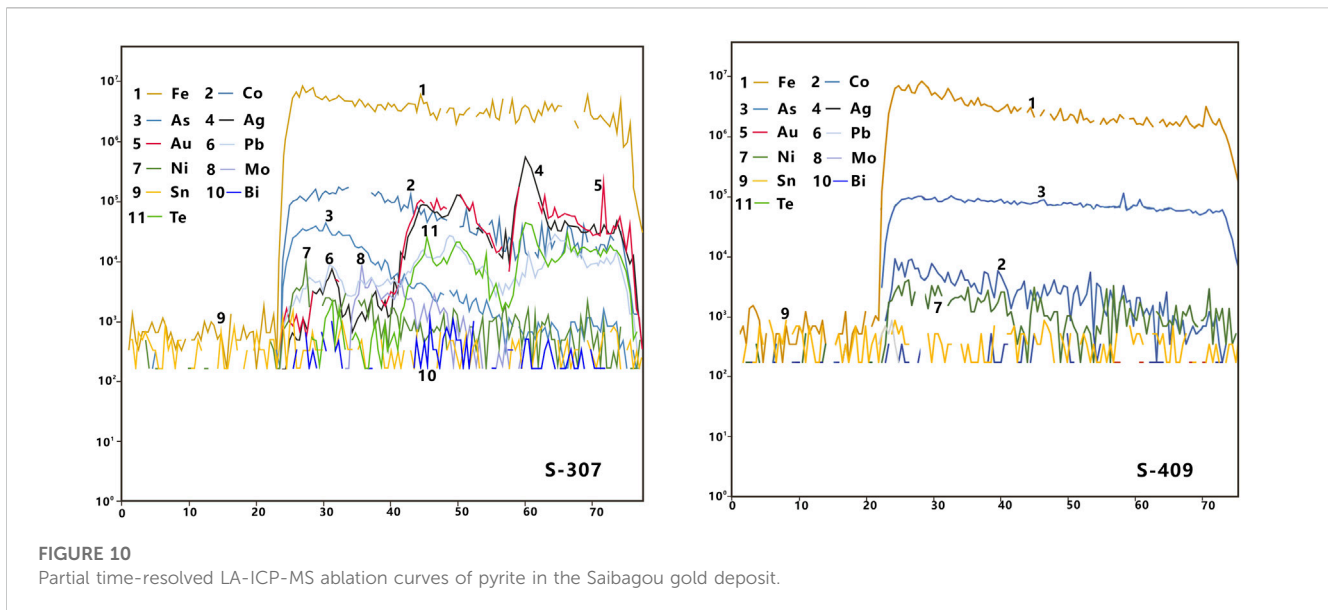
FIGURE 10
Partial time-resolved LA-ICP-MS ablation curves of pyrite in the Saibagou gold deposit.

These phenomena further indicate that the ore-forming fluids of the Saibagou gold deposit are As-bearing fluids. As revealed by the time-resolved LA-ICP-MS ablation curves of pyrite, the signals of Mo and Bi frequently varied with the Pb signal, and anomalous Pb peaks were frequently accompanied by the Mo and Bi peaks. In addition, galena trapped in pyrite grains was discovered under the microscope, indicating that Mo and Bi might be present as the micro-inclusions of Mo-Bi sulfides in the galena.
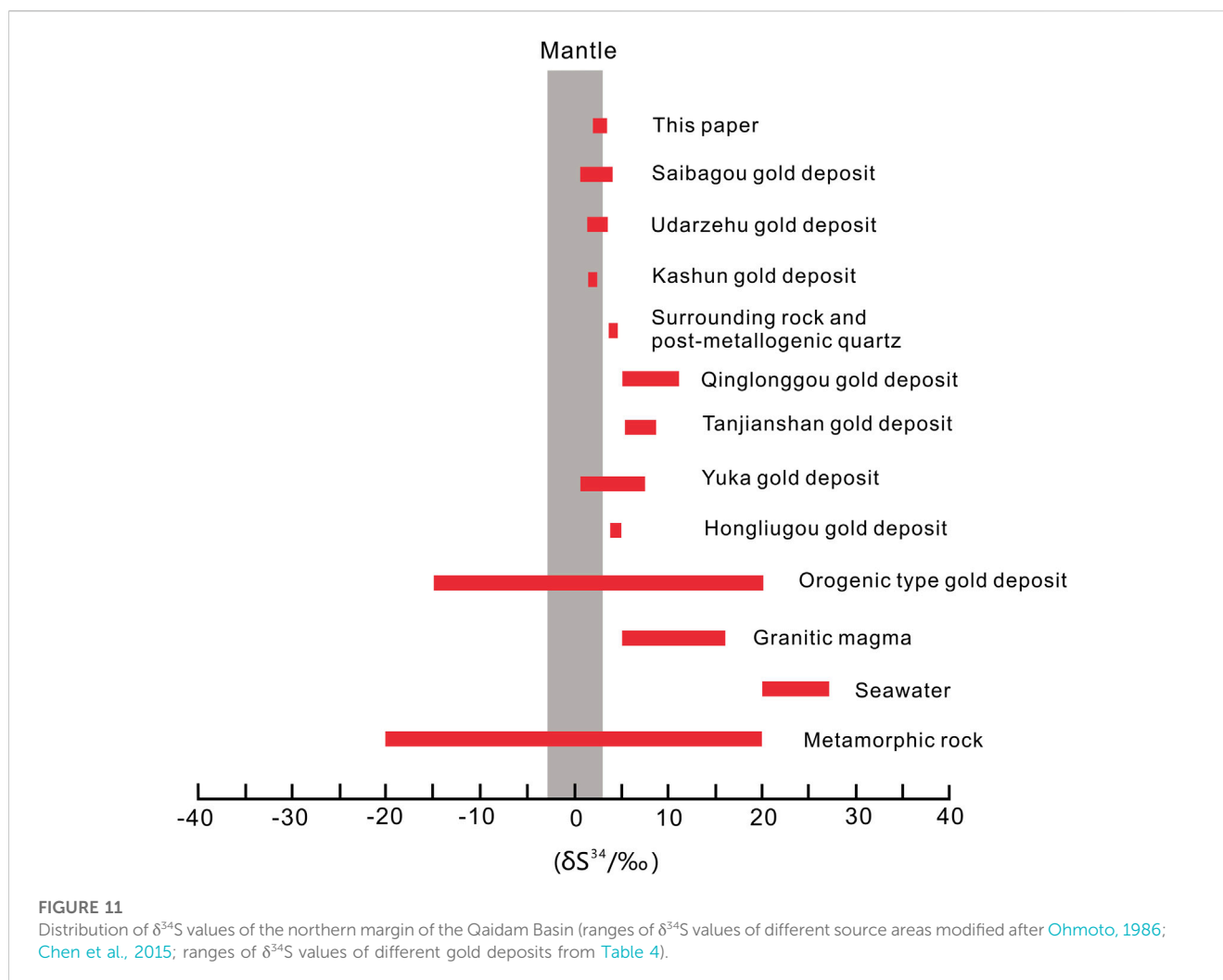
Pyrite in the quartz vein-type gold ores developed relatively slowly, resulting in relatively low trace element concentrations inside. Nevertheless, pyrite directly crystallized and precipitated in the ore-forming fluids, being free from the interference by other impurity elements. As a result, pyrite can effectively reflect the properties of the ore-forming fluids (Zhen et al., 2020). The pyrite in gold-bearing quartz vein-type ores in the Saibagou gold deposit has Co concentrations of 0.82 ppm–115.10 ppm, which are less than the maximum Co concentrations (1000 ppm) observed in the pyrite of mesothermal deposits (Roman et al., 2019). Furthermore, the pyrite has Ni concentrations of 0.60 ppm–19.29 ppm. Therefore, the Co and Ni concentrations in the pyrite are both less than 200 ppm and exactly fall within the ranges of those in acidic magmatic fluids (Tao et al., 2020). Many mesothermal-epithermal minerals, such as pyrite, chalcopyrite, galena, and sphalerite, have also been discovered in the Saibagou gold deposit. The fluid inclusions within the veins of the Saibagou gold deposit have homogeneous temperatures of mostly 160 C–350°C, indicating that the ore-forming fluids might be derived from acidic magmas and are moderate-to low-temperature As-bearing fluids.

6.4 Sources of ore-forming materials

Pyrite plays a significant role in the Saibagou gold deposit as one of the primary gold-bearing sulfides. Its characteristics, such as morphology, size, and elemental composition, provide valuable insights into the formation of gold in ores. In some specific geological environments, pyrite can be used to determine the properties of ore-forming fluids and the source of deposit materials (Ohmoto, 1986; Lu et al., 2022). As indicated by previous studies, the Saibagou gold deposit is a typical hydrothermal deposit (Liu et al., 2005). The sulfur isotopic composition in this deposit is closely related to the mineral crystallization temperature, isotopic composition, pH, and oxygen fugacity of hydrothermal fluids. The sulfides in the Saibagou gold deposit primarily include pyrite, chalcopyrite, galena, pyrrhotite, and sphalerite, with the absence of sulfate minerals. The alterations in the surrounding rocks are dominated by moderate-to low-temperature alterations, such as silicification and the alterations of pyrite, chlorite, and sericite. The fluid inclusions in the veins of the gold deposit have homogeneous temperatures of mostly 160 C–350 C (Liu et al., 2005). Accordingly, it can be inferred that the ore-forming hydrothermal fluids of the Saibagou gold deposit might have originated from a moderate-to low-temperature environment with a low oxygen fugacity. The S element in the ore-forming fluids of the Saibagou gold deposit mainly occurs as HS^- and S^{2-} ions, and the pyrite precipitating from fluids has similar $\delta^{34}S$ values to the ore-forming fluids (Ohmoto, 1972; Zhen et al., 2020). Therefore, it is feasible to use the sulfur isotopes of pyrite to indicate the characteristics of sulfur isotopes in the ore-forming fluids and determine the sources of ore-forming materials in the Saibagou gold deposit.

There are three main sources of sulfur on earth, namely, mantle-derived (magmatic) sulfur, seawater sulfur, and sedimentary sulfur (Ohmoto, 1986; Chaussidon and Lorand, 1990; Chen et al., 2015). As indicated by the geochemical characteristics of pyrite in the Saibagou gold deposit, pyrite formed at different metallogenic stages shows relatively concentrated $\delta^{34}S$ values of 1.99 ‰–3.28‰, with an average of 2.54‰ and an extreme difference of 1.29‰. The highly homogeneous $\delta^{34}S$ values indicate significant characteristics of mantle-derived sulfur (Ohmoto, 1986). In the Saibagou area and its adjacent regions, gold ores exhibit $\delta^{34}S$ values of 0.50 ‰–3.92‰, with an extreme difference of 3.42‰. The quartz veins bearing no gold ores (formed after the metallogenic period) and the surrounding rocks have $\delta^{34}S$ values of 3.7 ‰–4.00‰ (Zhang

FIGURE 11
Distribution of δ³⁴S values of the northern margin of the Qaidam Basin (ranges of δ³⁴S values of different source areas modified after Ohmoto, 1986; Chen et al., 2015; ranges of δ³⁴S values of different gold deposits from Table 4).

et al., 2001; Tang et al., 2021b). Gold deposits in the western part of the tectonic belt at the northern margin of the Qaidam Basin, such as Hongliugou, Tanjianshan, Yuka, and Qinglonggou (Guo and Shuwang, 1998; Fan, 2017; Zhang, 2017), have δ³⁴S values of 0.50 ‰–11.00‰ (extreme difference: 10.5‰), which are significantly higher than those in the eastern part of the tectonic belt. Although the δ³⁴S values of the gold deposits in the tectonic belt at the northern margin of the Qaidam Basin all fall within the range of the δ³⁴S values of orogenic gold deposits (Liu et al., 2021), the gold deposits in the eastern and western parts of the tectonic belt have greatly different sources of ore-forming materials. The relatively high δ³⁴S values of the gold deposits in the western part of the northern Qaidam Basin tectonic belt indicate that the ore-forming fluids underwent substantial water-rock interactions with the surrounding rocks near the pathway as they ascended, thus significantly increasing the δ³⁴S values of the fluids a phenomenon commonly observed in orogenic gold deposits (Hodkiewicz et al., 2009; Liu et al., 2021; Sugiono et al., 2021). The relatively low δ³⁴S values of gold deposits in the study area indicate that the chlorite alteration in shear zones served as a barrier to the migration of ore-forming minerals in hydrothermal fluids, hindering the water-rock interactions between the ore-forming

fluids and the surrounding rocks in the pathway (Wang et al., 2022) (Figure 11). As shown in this study, the gold-bearing quartz vein-type ores in the Saibagou gold deposit have δ³⁴S values of 1.99 ‰–3.28‰, with an average of 2.54‰ and an extreme differences is 1.29‰. These highly homogeneous δ³⁴S values are concentrated within the δ³⁴S range of mantle-derived sulfur (0‰±3‰), suggesting significant characteristics of mantle-derived sulfur. This result indicates that the surrounding rocks of ore bodies had a minor influence on the ore-forming fluids during the metallogenic process. Therefore, it can be inferred that the ore-forming materials of the Saibagou gold deposit mainly include mantle-derived materials in the deep earth.

7 Conclusion

Compared with the magmatic zircons in the gold ore samples, the hydrothermal zircons of the Saibagou gold deposit are significantly rich in LREEs. As indicated by the hydrothermal zircon ages of gold-bearing quartz vein-type ores, the Saibagou gold deposit in the study area is a superimposed hydrothermal gold deposit with at least two

metallogenic periods, namely, 423.91 ± 4.5 Ma and 470.18 ± 4.92 Ma. The dominant metallogenic period is 423.91 ± 4.5 Ma, which is slightly later than the age of the NWW-trending ductile-brittle shear zone in the mining area (426 Ma). In contrast, the secondary metallogenic period is 470.18 ± 4.92 Ma, of which the orebodies have a smaller scale and a lower gold grade than those of the dominant metallogenic period. This result indicates that the dating results of the hydrothermal zircons in the gold-bearing quartz vein-type ores can accurately represent the actual metallogenic age of the Saibagou gold deposit.

The *in situ* LA-ICP-MS analysis of pyrite shows that most trace elements (except for Ag, As, Cu, Bi, Co, and Ni) in the pyrite grains from the gold-bearing quartz veins in the Saibagou gold deposit have low concentrations, which are below or near the detection limits. The low trace element concentrations in pyrite, the stable Co, Ni, and As concentrations, and the presence of large amounts of mesothermal-epithermal minerals (e.g., pyrite, chalcopyrite, galena, and sphalerite) in the gold ores jointly indicate that the ore-forming fluids moderate to low-temperature As-bearing fluids, which might be derived from acidic magma. Furthermore, these results suggest that Ag, Zn, Cu, Bi, Co and Ni can serve as the near-orebody indicator elements for this deposit. This result indicates that the surrounding rocks of ore bodies had a minor influence on the ore-forming fluids during the metallogenic process. Therefore, it can be inferred that the ore-forming materials of the Saibagou gold deposit mainly include mantle-derived materials in the deep earth. It is feasible to use the sulfur isotopes of pyrite to indicate the characteristics of sulfur isotopes in the ore-forming fluids and determine the sources of ore-forming materials in the Saibagou gold deposit.

As indicated by the geochemical characteristics of pyrite in the Saibagou gold deposit, pyrite formed at different metallogenic stages has relatively concentrated $\delta^{34}S$ values of 1.99 ‰–3.28‰, with an average of 2.54‰ and an extreme difference of 1.29‰. These highly homogeneous $\delta^{34}S$ values concentrated in the $\delta^{34}S$ range of mantle-derived sulfur (0‰±3‰). This result suggests that the surrounding rocks of the ore bodies had minimal influence on the properties of the ore-forming fluids during the formation of the Saibagou gold deposit. However, it is noteworthy that the sulfur isotope values vary with the change of metallogenic period, and the change order of $\delta^{34}S_I < \delta^{34}S_{II} < \delta^{34}S_{III}$. According to the equilibrium fractionation curve of sulfur isotope exchange, the quantity of sulfur isotopes in pyrite increases as temperature decreases, This suggests that the sulfur isotope values increased as the temperature of gold mineralization decreased.

Data availability statement

The original contributions presented in the study are included in the article/Supplementary material, further inquiries can be directed to the corresponding author.

Author contributions

JX: conceptualization, writing—original draft, Software, formal analysis and data curation. JW: conceptualization, writing—review and editing, funding acquisition, supervision, project administration, the fieldwork, the experiment and data curation. JbL: methodology, supervision. YL: resources, visualization. KB: resources, validation. JwL: visualization. LC: supervision. SW: investigation, software. All authors contributed to manuscript revision and approved the submitted version.

Conflict of interest

The authors declare that the research was conducted in the absence of any commercial or financial relationships that could be construed as a potential conflict of interest.

Publisher's note

All claims expressed in this article are solely those of the authors and do not necessarily represent those of their affiliated organizations, or those of the publisher, the editors and the reviewers. Any product that may be evaluated in this article, or claim that may be made by its manufacturer, is not guaranteed or endorsed by the publisher.

References

Baatartsogt, B., Wagner, T., Taubald, H., Mierdel, K., and Markl, G. (2007). Hydrogen isotope determination of fluid inclusion water from hydrothermal fluorite: Constraining the effect of the extraction technique. *Chem. Geol.* 244 (3-4), 474–482. doi:10.1016/j.chemgeo.2007.06.031

Belousova, E. A., Griffin, W. L., and O'Reilly, S. Y. (2006). Zircon crystal morphology, trace element signatures and Hf isotope composition as a tool for petrogenetic modelling: Examples from eastern Australian granitoids. *J. Petrol.* 47 (2), 329–353. doi:10.1093/petrology/egi077

Berner, Z. A., Puchelt, H., Noeltner, T., and Kramar, U. (2013). Pyrite geochemistry in the toarcian posidonia shale of south-west Germany: Evidence for contrasting trace-element patterns of diagenetic and syngenetic pyrites: *Pyrite*

element geochemistry. *Sedimentology* 60 (2), 548–573. doi:10.1111/j.1365-3091.2012.01350.x

Cai, P. J., Xu, R. K., Zheng, Y. Y., Yin, Y., Chen, X., Fan, X., et al. (2019). Fluid inclusion and H–O–S–Pb isotope geochemistry of the Yuka orogenic gold deposit, northern Qaidam, China. *Geofluids* 2019, 1–17. doi:10.1155/2019/6912519

Cao, B., Yan, Z., and Fu, C. L. (2019). Component and deformation of the Saibagou accretionary complex in the northern margin of the Qaidam block. *Acta Petrol. Sin.* 35 (4), 1015–1032.

Chaussidon, M., and Lorand, J. P. (1990). Sulphur isotope composition of orogenic spinel lherzolite massifs from Ariege (North-Eastern Pyrenees, France): An ion

microprobe study. *Geochim. Cosmochim. Acta* 54 (10), 2835–2846. doi:10.1016/0016-7037(90)90018-g

Chen, N. S., Wang, Q. Y., and Chen, Q. (2007). Components and metamorphism of the basements of the Qaidam and Oulongbuluke micro-continental blocks, and a tentative interpretation of paleocontinental evolution in NW-Central China. *Earth Sci. Front.* (1), 43–55.

Chen, M. H., Zhang, Z. Q., Santosh, M., Dang, Y., and Zhang, W. (2015). The carlin-type gold deposits of the "golden triangle" of SW China: Pb and S isotopic constraints for the ore geGenesis. *J. Asian Earth Sci.* 103, 115–128. doi:10.1016/j.jseaes.2014.08.022

Chen, X., Xu, R. K., Schertl, H. P., and Zheng, Y. (2018a). Eclogite-facies metamorphism in impure marble from north Qaidam orogenic belt: Geodynamic implications for early Paleozoic continental-arc collision. *Lithos* 310, 201–224. doi:10.1016/j.lithos.2018.04.005

Chen, X., Xu, R. K., Zheng, Y. Y., and Cai, P. (2018b). Petrology and geochemistry of high niobium eclogite in the North Qaidam orogen, Western China: Implications for an eclogite facies metamorphosed island arc slice. *J. Asian Earth Sci.* 164, 380–397. doi:10.1016/j.jseaes.2018.07.003

Chen, Y., Liu, G., Zhou, C., Zhou, H., Wei, Y., and Liu, Y. (2023). The influence of gold mining wastes on the migration-transformation behavior and health risks of arsenic in the surrounding soil of mined-area. *Front. Earth Sci.* 10, 1068763.

Claoue, J. C., King, R. W., and Kerrich, R. (1990). Archaean hydrothermal zircon in the Abitibi greenstone belt: Constraints on the timing of gold mineralisation. *Earth Planet. Sci. Lett.* 98 (1), 109–128. doi:10.1016/0012-821x(90)90091-b

Claoue, J. C., King, R. W., and Kerrich, R. (1992). Reply to comment by F. Corfu and D.W. Davis on "archaean hydrothermal zircon in the Abitibi greenstone belt: Constraints on the timing of gold mineralisation". *Earth Planet. Sci. Lett.* 109 (3-4), 601–609. doi:10.1016/0012-821x(92)90118-f

Clauer, N., Savin, S. M., and Chaudhuri, S. (1992). Isotopic compositions of clay minerals as indicators of the timing and conditions of sedimentation and burial diagenesis. *Lect. Notes Earth Sci.* 43, 239–286.

Fan, X. B. (2017). *A discussion on genesis of yuqia gold deposit in da chaidan of Qinghai Province*. Beijing: China University of Geosciences.

Feng, C. Y., Zhang, D. Q., Li, D. X., and Cui, Y. H. (2002). Geological characteristics and Ore-forming age of the Saibagou gold deposit, Qinghai province. *Mineral. Deposits* (1), 45–52.

Franchini, M., McFarlane, C., Maydagán, L., Reich, M., Lentz, D. R., Meinert, L., et al. (2015). Trace metals in pyrite and marcasite from the Agua Rica porphyry-high sulfidation epithermal deposit, Catamarca, Argentina: Textural features and metal zoning at the porphyry to epithermal transition. *Ore Geol. Rev.* 66, 366–387. doi:10.1016/j.oregeorev.2014.10.022

Fu, Q. Y., and Li, B. L. (1998). Metallogenetic features and Ore-controllinc conditions of saibagou gold deposit, Qinghai. *Qinghai Geol.* (1), 43–49.

Fu, J. L., Hu, Z. C., Zhang, W., Yang, L., Liu, Y., Li, M., et al. (2016). *In situ* sulfur isotopes (δ^{34}S and δ^{33}S) analyses in sulfides and elemental sulfur using high sensitivity cones combined with the addition of nitrogen by laser ablation MC-ICP-MS. *Anal. Chim. Acta* 911, 14–26. doi:10.1016/j.aca.2016.01.026

Gao, W., Hu, R. Z., Hofstra, A. H., Li, Q., Zhu, J., Peng, K., et al. (2021). U-Pb dating on hydrothermal rutile and monazite from the badu gold deposit supports an early cretaceous age for carlin-type gold mineralization in the youjiang basin, southwestern China. *Econ. Geol.* 116 (6), 1355–1385. doi:10.5382/econgeo.4824

Geisler, T., Rashwan, A. A., Rahn, M. K. W., Poller, U., Zwingmann, H., Pidgeon, R. T., et al. (2003). Low-temperature hydrothermal alteration of natural metamict zircons from the Eastern Desert, Egypt. *Mineral. Mag.* 67 (3), 485–508. doi:10.1180/0026461036730112

Goldfarb, R. J., and Groves, D. I. (2015). Orogenic gold: Common or evolving fluid and metal sources through time. *Lithos* 233, 2–26. doi:10.1016/j.lithos.2015.07.011

Goldfarb, R. J., Groves, D. I., and Gardoll, S. (2001). Orogenic gold and geologic time: A global synthesis. *Ore Geol. Rev.* 18 (1-2), 1–75. doi:10.1016/s0169-1368(01)00016-6

Gregory, D. D., Large, R. R., Bath, A. B., Steadman, J. A., Wu, S., Danyushevsky, L., et al. (2016). Trace element content of pyrite from the kapai slate, st. Ives gold district, western Australia. *Econ. Geol.* 111 (6), 1297–1320. doi:10.2113/econgeo.111.6.1297

Guo, J. H., and Shuwang, C. (1998). Origin of the ore-forming matter of tanjianshan gold field, Qinghai province. *J. Precious Metallic Geol.* 7 (3), 189–204. doi:10.13686/j.cnki.dzyzy.1998.03.004

Hodkiewicz, P. F., Groves, D. I., Davidson, G. J., Weinberg, R. F., and Hagemann, S. G. (2009). Influence of structural setting on sulphur isotopes in Archean orogenic gold deposits, Eastern Goldfields Province, Yilgarn, Western Australia. *Miner. Deposita* 44 (2), 129–150. doi:10.1007/s00126-008-0211-5

Hoskin, P. W. O., and Ireland, T. R. (2000). Rare Earth element chemistry of zircon and its use as a provenance indicator. *Geology* 28 (7), 627–630. doi:10.1130/0091-7613(2000)028<0627:reecoz>2.3.co;2

Hoskin, P. W. O., and Schaltegger, U. (2003). The composition of zircon and igneous and metamorphic petrogenesis. *Rev. Mineral. Geochem.* 53 (1), 27–62. doi:10.2113/0530027

Hoskin, P. W. O. (2005). Trace-element composition of hydrothermal zircon and the alteration of Hadean zircon from the Jack Hills, Australia. *Geochim. Cosmochim. Acta* 69 (3), 637–648. doi:10.1016/j.gca.2004.07.006

Hu, Z. C., Zhang, W., Liu, Y. S., Gao, S., Li, M., Zong, K., et al. (2015). "Wave" signal-smoothing and mercury-removing device for laser ablation quadrupole and multiple collector ICPMS analysis: Application to lead isotope analysis. *Anal. Chem.* 87 (2), 1152–1157. doi:10.1021/ac503749k

Huang, H. X., Luosang, J., Dai, Z. W., Liu, H., and Fu, J. (2021). Hydrothermal zircon geochronology in the shangxu gold deposit and its implication for the early cretaceous orogenic gold mineralization in the Middle bangonghu–nujiang suture zone. *Acta Geol. Sinica-English Ed.* 95 (4), 1249–1259. doi:10.1111/1755-6724.14679

Kerrich, R., and Kyser, T. K. (1994). 100 Ma timing paradox of Archean gold, Abitibi greenstone belt (Canada): New evidence from U-Pb and Pb-Pb evaporation ages of hydrothermal zircons. *Geology* 22 (12), 1131–1134. doi:10.1130/0091-7613(1994)022<1131:mtpoag>2.3.co;2

Large, R. R., Danyushevsky, L., Hollit, C., Maslennikov, V., Meffre, S., Gilbert, S., et al. (2009). Gold and trace element zonation in pyrite using a laser imaging technique: Implications for the timing of gold in orogenic and carlin-style sediment-hosted deposits. *Econ. Geol.* 104 (5), 635–668. doi:10.2113/gsecongeo.104.5.635

Li, C., Li, L., Li, S. R., Santosh, M., and Shen, J. F. (2022). Geochemistry of hydrothermal zircon as a proxy to fingerprint ore fluids in late Mesozoic dracatonic gold deposits. *Ore Geol. Rev.* 143, 104703. doi:10.1016/j.oregeorev.2022.104703

Li, H., Zhu, D. P., Algeo, T. J., Li, M., Jiang, W. C., Chen, S. F., et al. (2022). Pyrite trace element and S-Pb isotopic evidence for contrasting sources of metals and ligands during superimposed hydrothermal events in the Dongping gold deposit, North China. *Miner. Deposita*, 1–22.

Liu, Z. T., Ren, J. Q., and Yang, Y. Z. (2005). *Gold deposits in Qinghai Province*. Beijing: Geology Press, 1–374. (in Chinese with English abstract).

Liu, Y. S., Hu, Z. C., Gao, S., Günther, D., and Xu, J. (2008). *In situ* analysis of major and trace elements of anhydrous minerals by LA-ICP-MS without applying an internal standard. *Chem. Geol.* 257 (1-2), 34–43. doi:10.1016/j.chemgeo.2008.08.004

Liu, Y. S., Gao, S., Hu, Z. C., Gao, C., Zong, K., and Wang, D. (2010). Continental and oceanic crust recycling-induced melt-peridotite interactions in the trans-north China orogen: U-Pb dating, Hf isotopes and trace elements in zircons from mantle xenoliths. *J. Petrol.* 51 (1-2), 537–571. doi:10.1093/petrology/egp082

Liu, Z. K., Mao, X. C., Deng, H., Li, B., Zhang, S., Lai, J., et al. (2018). Hydrothermal processes at the Axi epithermal Au deposit, Western Tianshan: Insights from geochemical effects of alteration, mineralization and trace elements in pyrite. *Ore Geol. Rev.* 102, 368–385. doi:10.1016/j.oregeorev.2018.09.009

Liu, J., Cai, P. J., Zeng, X. H., and Liu, L. (2021). Geology, ore-forming fluid and metallogenic age of orogenic gold deposits in the Northern Qaidam. *Geol. China* 48 (2), 374–387.

Lu, J. L., Fan, Y. C., Yin, Y. C., Xiong, Y., Guo, J., Tian, W., et al. (2022). Metal source of gold deposits in the Jiaoxibei area, Eastern China: Insights from trace element analysis of gold and pyrite. *Resour. Geol.* 72 (1), e12278. doi:10.1111/rge.12278

Luo, Z. K., Miao, L. C., and Guan, K. (2000). Discussion on the metallogenetic epoch of gold deposit on north fringe of North China platform. *Gold Geol.* (2), 65–71.

Ma, Y., Jiang, S. Y., and Frimmel, H. E. (2022). Metallogeny of the Late Jurassic Qiucun epithermal gold deposit in southeastern China: Constraints from geochronology, fluid inclusions, and H-O-C-Pb isotopes. *Ore Geol. Rev.* 142, 104688. doi:10.1016/j.oregeorev.2021.104688

Ohmoto, H. (1972). Systematics of sulfur and carbon isotopes in hydrothermal ore deposits. *Econ. Geol.* 67 (5), 551–578. doi:10.2113/gsecongeo.67.5.551

Ohmoto, H. (1986). Stable isotope geochemistry of ore deposits. *Rev. Mineral. Geochem.* 16 (1), 491–559.

Reich, M., Kesler, S. E., Utsunomiya, S., Palenik, C. S., Chryssoulis, S. L., and Ewing, R. C. (2005). Solubility of gold in arsenian pyrite. *Geochim. Cosmochim. Acta* 69 (11), 2781–2796. doi:10.1016/j.gca.2005.01.011

Roman, N., Reich, M., Leisen, M., Morata, D., Barra, F., and Deditius, A. P. (2019). Geochemical and micro-textural fingerprints of boiling in pyrite. *Geochim. Cosmochim. Acta* 246, 60–85. doi:10.1016/j.gca.2018.11.034

Rubatto, D., and Hermann, J. (2003). Zircon formation during fluid circulation in eclogites (monviso, western alps): Implications for Zr and Hf budget in subduction zones. *Geochim. Cosmochim. Acta* 67 (12), 2173–2187. doi:10.1016/s0016-7037(02)01321-2

Rubatto, D. (2002). Zircon trace element geochemistry: Partitioning with garnet and the link between U–Pb ages and metamorphism. *Chem. Geol.* 184 (1-2), 123–138. doi:10.1016/s0009-2541(01)00355-2

Schaltegger, U. (2007). Hydrothermal zircon. *Elements* 3 (1), 51–79. doi:10.2113/gselements.3.1.51

Shao, P. C., Chen, S. Y., and Sun, J. P. (2018). Shrimp zircon U-Pb dating and petro-geochemistry of aolaoshan gabbro-diorite in the western north margin of Qaidam basion. *Acta Geol. Sin.* 92 (9), 1888–1903.

Smythe, D. J., and Brenan, J. M. (2016). Magmatic oxygen fugacity estimated using zircon-melt partitioning of cerium. *Earth Planet. Sci. Lett.* 453, 260–266. doi:10.1016/j.epsl.2016.08.013

Song, S. G., Niu, Y. L., Su, L., Zhang, C., and Zhang, L. (2014). Continental orogenesis from ocean subduction, continent collision/subduction, to orogen collapse, and orogen recycling: The example of the North Qaidam UHPM belt, NW China. *Earth-Sci. Rev.* 129, 59–84. doi:10.1016/j.earscirev.2013.11.010

Sugiono, D., Thébaud, N., LaFlamme, C., Fiorentini, M., Martin, L., Rogers, J., et al. (2021). Integration of multiple sulfur isotopes with structural analysis unveils the evolution of ore fluids and source of sulfur at the Kanowna Belle Archean orogenic gold deposit, Yilgarn Craton, Western Australia. *Miner. Deposita* 56 (8), 1471–1490. doi:10.1007/s00126-020-01032-1

Tang, M. Y., Ding, Z. J., and Zhu, D. Q. (2021a). On discovery and origin of tellurides in the saibagou gold deposit in the northern margin of Qaidam basin. *Acta Geol. Sin.* 95 (12), 3778–3789.

Tang, M. Y., He, Z. W., and Zhu, D. Q. (2021b). S and Pb isotopic compositions in Saibagou gold deposit on north margin of Qaidam Basin: An indication to the source of metallogenic materials. *Mineral. Deposits* 40 (1), 117–127.

Tao, L. X., Zhen, S. M., Bai, H. J., Wang, J., Wang, D. Z., Zha, Z. J., et al. (2020). Pyrite trace element composition and S-Pb isotope characters of the dabaiyang gold deposit, hebei province. *J. Jilin Univ. Sci. Ed.* 50 (5), 1582–1598.

Tong, H. K., Zhang, S. G., Xu, G. W., and Huang, Y. B. (2009). Characteristics and Genesis of ductile shear zone related gold deposits in Saibagou of Wulan County. *Northwest. Geol.* 42 (1), 88–94.

Vallance, J., Boiron, M. C., Cathelineau, M., Marignac, C., and Boiron, M. C. (2004). The granite hosted gold deposit of moulin de Chéni (Saint-Yrieix district, massif central, France): Petrographic, structural, fluid inclusion and oxygen isotope constraints. *Miner. Deposita* 39 (3), 265–281. doi:10.1007/s00126-003-0396-6

Vavra, G., Schmid, R., and Gebauer, D. (1999). Internal morphology, habit and U-Th-Pb microanalysis of amphibolite-to-granulite facies zircons: Geochronology of the ivrea zone (southern alps). *Contributions Mineral. Petrol.* 134 (4), 380–404. doi:10.1007/s004100050492

Wang, W. X., Tang, M. Y., and Ding, Z. J. (2022). Deep hydrothermal alteration of the Saibagou gold deposit in the northern margin of the Qaidam Basin. *Geol. Explor.* 58 (5), 917–928.

Wu, C. L., Wooden, J. L., Yang, J. S., Robinson, P. T., Lingsen, Z., Rendeng, S., et al. (2006). Granitic magmatism in the north Qaidam early paleozoic ultrahigh-pressure metamorphic belt, northwest China. *Int. Geol. Rev.* 48 (3), 223–240. doi:10.2747/0020-6814.48.3.223

Wu, H. B., Wang, W. X., Zheng, C. L., Zhu, D., Tang, M., Xin, Z., et al. (2022). Zircon U-Pb age, geochemical characteristics and geological significance of tonalite in saibagou gold deposit, the northern margin of Qaidam. *Northwest. Geol.* 55 (1), 101–113.

Yang, J. S., Wu, C. L., Zhang, J. X., Shi, R., Meng, F., Wooden, J., et al. (2006). Protolith of eclogites in the north Qaidam and Altun UHP terrane, NW China: Earlier oceanic crust? *J. Asian Earth Sci.* 28 (2-3), 185–204. doi:10.1016/j.jseaes.2005.09.020

Ye, T. Z., Liu, Z. C., and Pang, Z. S. (2014). *Prediction theory and method of prospecting in exploration area (general theory).* Beijing: Geology Press, 1–593. (in Chinese with English abstract).

Yu, J. Z., Zheng, Y. Y., and Xu, R. K. (2020). LA-ICP-MS zircon U-Pb age of the host rock and hydrothermal zircon in gold-bearing quartz vein of shuangkoushan Au-Ag-Pb deposit, north Qaidam: Limitation for the mineralization age and implication for the Genesis of the deposit. *Acta Geol. Sin.* 94 (11), 3361–3375.

Zhang, S. H., Zhou, X. Q., and Tian, X. J. (2001). Stably isotopic composition and its geological significance in tomorite gold deposit, wulan county, Qinghai province. *Geol. Explor.* (5), 10–14.

Zhang, D. Q., Dang, X. Y., She, H. Q., Li, D. X., Feng, C. Y., Li, J. W., et al. (2005). Ar-Ar dating of orogenic gold deposits in northern margin of Qaidam and East Kunlun Mountains and its geological significance. *Mineral. Deposits* (2), 87–98.

Zhang, J. X., Yang, J. S., Meng, F. C., Yusheng, W., Huimin, L., and Cailai, W. (2006). U–Pb isotopic studies of eclogites and their host gneisses in the Xitieshan area of the North Qaidam mountains, Western China: New evidence for an early Paleozoic HP–UHP metamorphic belt. *J. Asian Earth Sci.* 28 (2-3), 143–150. doi:10.1016/j.jseaes.2005.09.017

Zhang, Y. Y., Wang, Q. M., Ren, R. P., and Lu, F. (2018). Metallogenic geological characteristics and prospecting direction of the Saibagou area in Wulan county, Qinghai Province. *North China Geol.* 41 (3), 191–197.

Zhang, D. Q., She, H. Q., Feng, C. Y., Daxin, L., and Jinwen, L. (2009). Geology, age, and fluid inclusions of the Tanjianshan gold deposit, Western China: Two orogenies and two gold mineralizing events. *Ore Geol. Rev.* 36 (1-3), 250–263. doi:10.1016/j.oregeorev.2009.06.002

Zhang, X. W., Xiang, H., Zhong, Z. Q., Zhou, H. W., Zhang, L., Yang, N., et al. (2009). U-Pb dating and trace elements composition of hydrothermal zircons from jianfengling granite, hainan: Restriction on the age of hydrothermal event and mineralization of Baolun gold deposit. *Earth Sci.* 34 (6), 921–930.

Zhang, Y. J. (2017). *Study on the metallogenesis of endogenous metallic deposits in tanjianshan area in Qinghai Province.* Changchun: Jilin University. 106–107, 117.

Zhen, S. M., Pang, Z. S., and Zhu, X. Q. (2020). The characteristics of trace elements and S, Pb, He and Ar isotopes in the Liyuan gold deposit in Shanxi Province, and their significance. *Earth Sci. Front.* 27 (2), 373–390.

Zheng, X., Sun, X., Li, Q., Jeon, H., and Zhou, T. C. (2020). Genesis of the Bangbu gold deposit in the southern Tibet: Evidenced from *in-situ* sulfur isotopes and trace element compositions of pyrite. *Ore Geol. Rev.* 126, 103591. doi:10.1016/j.oregeorev.2020.103591

Zhong, S. H., Feng, C. Y., Seltmann, R., Li, D., and Qu, H. (2018). Can magmatic zircon be distinguished from hydrothermal zircon by trace element composition? The effect of mineral inclusions on zircon trace element composition. *Lithos* 314, 646–657. doi:10.1016/j.lithos.2018.06.029

Zhou, X. P., Hu, B. Q., Zhou, M. L., Kang, K., Hu, L., Jiang, F., et al. (2022). Geological characteristics, zircon U-Pb age and its records for tectonomagmatic events of lamprophyres in Xilaokou gold deposit, northeast margin of Jiaolai Basin. *Geol. Bull. China* 41 (9), 1634–1647.

Zong, K. Q., Klemd, R., Yuan, Y., He, Z., Guo, J., Shi, X., et al. (2017). The assembly of Rodinia: The correlation of early Neoproterozoic (ca. 900 Ma) high-grade metamorphism and continental arc formation in the southern Beishan Orogen, southern Central Asian Orogenic Belt (CAOB) *Precambrian Res.* 290, 32–48. doi:10.1016/j.precamres.2016.12.010